

UNIVERSITY
OF AMSTERDAM



VRIJE
UNIVERSITEIT
AMSTERDAM

MSc Physics and Astronomy (joint degree)
Advanced Matter and Energy Physics track

Master Thesis

Photoassociation spectroscopy of an ultracold Rb-Sr mixture in an optical lattice

by

Tommaso Vedovello

First Supervisor:	Dr. N.J. van Druten
Second Supervisor:	Prof. Dr. F. Schreck
Daily supervisor:	Digvijay

Sep. 2025 — Aug. 2026

Van der Waals-Zeeman Institute
University of Amsterdam

a Maripì

Abstract

RbSr is a strongly polar ($d = 1.54\,\mathrm{D}$) and open-shell molecule attractive for quantum simulation, precision measurement and cold chemistry. Because Feshbach resonances between an alkali and a closed-shell atom are only a few mG wide, magnetoassociation is challenging, which motivates us to explore a less conventional strategies such as optical association. The ^{87}Rb–^{87}Sr isotopologue is the natural candidate: its interspecies scattering length of $1421\,a_0$ places the least bound state only $h \times 20.5\,\mathrm{kHz}$ below the continuum, comparable to optical-lattice trap frequencies and therefore within reach of a confinement-induced resonance. The same large scattering length, however, comes at the cost of large three-body recombination rate.

This thesis reports one-photon photoassociation spectroscopy of Rb–Sr in a one-dimensional optical lattice. I built the photoassociation laser system: an injection-locked diode delivering 150 mW at 689 nm, followed by two double-pass acousto-optic modulators that generate the free-bound and bound-bound frequencies. The injection bandwidth of the diode was characterized against diode temperature and seed power. In addition, we solved a persistent problem concerning the optical lattice: the measured lattice depth was a factor of five below the calculated value, in both parametric-heating and Kapitza-Dirac measurements. We traced the discrepancy down to a broadband phase-noise background in the fiber amplifier, identified with a purpose-built fringe-visibility interferometer. Replacing the amplifier restored the expected lattice frequencies. Confining the mixture to a quasi-two-dimensional geometry then suppresses three-body losses and extends its lifetime to several hundred milliseconds. Four known photoassociation lines of ^{87}Rb–^{88}Sr are reproduced, and the target ^{87}Rb–^{87}Sr line is measured with and without the lattice. The stabilizing effect of the lattice allows to get a better contrast even when shining the photoassociation light for half the time compared to the case without lattice, and decrease the linewidth from 13 to 6.6 MHz. These results are a promising starting point for producing weakly bound ^{87}Rb–^{88}Sr molecules and further pursuing the creation of the first ultracold groundstate alkali–alkaline-earth molecules.

Contents

1 Introduction **3**
- 1.1 Why RbSr molecules? . . . 3
- 1.2 Applications of ultracold polar molecules . . . 4
- 1.3 Thesis overview . . . 5

2 Experimental setup and methods **7**
- 2.1 The machine . . . 7
- 2.2 Rb Setup . . . 9
- 2.3 Sr setup . . . 10
  - 2.3.1 Sr level scheme . . . 10
  - 2.3.2 Sr laser system . . . 12
- 2.4 Rb–Sr ultracold mixture . . . 14
- 2.5 Experimental sequence . . . 16
  - 2.5.1 Rb cooling sequence . . . 17
  - 2.5.2 Sr cooling sequence . . . 17
  - 2.5.3 Sympathetic cooling and evaporation . . . 19
  - 2.5.4 Creation of the mixture and photoassociation . . . 20

3 1D optical lattice **22**
- 3.1 Motivation . . . 22
  - 3.1.1 Confinement induced stabilization of the mixture . . . 22
  - 3.1.2 Confinement induced resonance . . . 23
- 3.2 Theory of optical lattices . . . 24
  - 3.2.1 Optical dipole traps . . . 24
  - 3.2.2 Optical lattice . . . 26
- 3.3 Lattice characterization methods . . . 27
  - 3.3.1 Parametric heating . . . 27
  - 3.3.2 Kapitza-Dirac BEC diffraction in Bragg regime . . . 28
- 3.4 Debugging sequence . . . 30
  - 3.4.1 Lateral displacement prism and fringes method . . . 34
  - 3.4.2 Phase noise characterization . . . 37

4 Photo-association spectroscopy **39**
- 4.1 Single photon PA spectroscopy . . . 39
- 4.2 Two-photon PA spectroscopy . . . 40
- 4.3 Experimental setup for PA spectroscopy . . . 42
  - 4.3.1 Injection locked laser . . . 43

4.3.2 Optical setup 46
4.4 One-photon spectroscopy results 47
4.4.1 PA spectroscopy of ^{87}Rb–^{88}Sr 48
4.4.2 PA spectroscopy of ^{87}Rb–^{87}Sr 50
4.5 Next steps 51

5 Conclusions and outlook **54**

Chapter 1

Introduction

1.1 Why RbSr molecules?

Over the last three decades ultracold quantum gases have become one of the most versatile platforms of modern physics. A single trapped atomic species already offers a remarkable degree of control over temperature, density, internal state and confining potential; adding a *second* species increases the number of available "knobs". The two components of an ultracold mixture can be chosen with any combination of quantum statistics – Bose-Bose, Bose-Fermi or Fermi-Fermi – with huge range of mass ratios. The resulting interplay between statistics, mass imbalance and scattering lengths gives access to a broad range of few- and many-body phenomena [1, 2]. In addition, an ultracold mixture is the necessary starting point of every experiment that aims to assemble molecules from atoms.

Molecules are attractive because they possess more degrees of freedom with respect to atoms. On top of the electronic and hyperfine structure, they rotate and vibrate, and a heteronuclear molecule carries a permanent electric dipole moment due to the different electronegativity of the nuclei. Once the molecules are polarized by an external field, this dipole moment translates into long-range, anisotropic and tunable dipole-dipole interactions. The same rich internal structure, however, is what makes molecules so hard to cool. Laser cooling relies on closed cycling transitions, and these are essentially absent in molecules: after an electronic excitation the molecule decays into a whole ladder of rovibrational levels that the cooling laser no longer addresses. Direct laser cooling is nonetheless possible, exploiting a cryogenic buffer gas cooling source and a large number of repumping lasers, but it currently reaches phase-space densities of order 10^{-6} [3], still many orders of magnitude away from quantum degeneracy. The alternative route, the one followed in this laboratory, is to first cool the atoms, then assemble the molecule. A pair of atoms is associated into a weakly bound state and is subsequently transferred to a bound rovibrational level by a coherent two-photon process. This strategy produced degenerate Fermi gas of KRb molecules [4]. An intermediate approach allowed to associate NaCs molecules at 700 nK and then induce an effective repulsive interaction and perform evaporative cooling up to degeneracy, creating the first BEC of dipolar molecules [5]. To this date, however, every polar molecule assembled from ultracold atoms is a bialkali dimer, whose $^1\Sigma^+$ electronic ground state is closed-shell and therefore almost insensitive to magnetic fields.

RbSr belongs to a different class. Combining an alkaline atom with an alkaline-earth atom, yields a $^2\Sigma^+$ electronic ground state, i.e. a molecule that is at the same time *strongly polar* and *open-shell*. Its permanent electric dipole moment in the rovibrational ground state is $d = 1.54\,\mathrm{D}$ [6], and its unpaired electron gives it a magnetic moment of $1\,\mu_b$. The price to pay for Sr being closed shell is that it is much less sensitive to magnetic fields. The interspecies Feshbach resonances that make magnetoassociation so efficient in bi-alkali systems are here only a few mG wide. They were predicted [7] and eventually observed in this very apparatus [8], but they are practically hardly usable. On the other hand, a positive feature of alkaline-earth atoms is the number of available isotopes: three stable bosons and one fermion. This variety gives, in the case of strontium, more freedom in choosing the isotope with the best scattering properties with Rb.

The RbSr experiment at the Van der Waals-Zeeman Institute routinely produces doubly degenerate Rb–Sr mixtures [9], it provided the first observation of Feshbach resonances between an alkali and a closed-shell atom [8], and it delivered an accurate determination of the RbSr $^2\Sigma^+$ ground-state potential and of the scattering lengths of all its isotopologues [10]. Since those Feshbach resonances turned out to be too narrow to be useful for association, the current strategy is to associate the atom pair with light rather than with a magnetic field. The isotopic combination ^{87}Rb–^{87}Sr is the natural candidate, because its anomalously large interspecies scattering length of $1421\,a_0$ places the least bound state of the electronic ground-state potential only $h \times 20.5\,\mathrm{kHz}$ below the free atoms threshold, within reach of a confinement-induced resonance [11]. The work presented in this thesis is a step along that route.

1.2 Applications of ultracold polar molecules

Quantum simulation and computation. The rotational structure of polar molecules can be used both analogically and digitally, for quantum simulation and computation respectively [12]. Ultracold polar molecules pinned in an optical lattice are a natural analogue simulator of lattice spin models. The dipole-dipole interaction between molecules on neighboring sites mimics the interaction between electrons in a crystal.

The manifold of rotational states can encode not just a qubit but a qudit, and it is addressed coherently with cheap and spectrally pure microwave and radio-frequency sources. Rotational states have lifetimes far longer than any experimentally relevant timescale, and the dipole-dipole interaction provides the entangling gate between neighbouring molecules [13].

Precision measurements. Molecules are also exquisite probes of fundamental physics, precisely because their internal structure is so sensitive to the interactions between their constituents. The flagship example is the search for a permanent electric dipole moment of the electron (eEDM), a quantity that the Standard Model predicts to be immeasurably small but that many of its extensions predict to be within experimental reach; a non-zero result would be direct evidence of new physics, with implications for the matter-antimatter asymmetry. The advantage of polar, open-shell molecules is that the unpaired electron experiences the enormous internal field of the polarized molecule, up to a million times larger than any static laboratory

field. The best limits to date, $d_e < 1.1 \times 10^{-29}$ e·cm with ThO [14] and $d_e < 4.1 \times 10^{-30}$ e·cm with HfF^+ [15], were obtained with cold beams and trapped ions, and are ultimately limited by the interaction time. The next generation of experiments aims at large samples of ultracold molecules held in an optical lattice [16], where coherence times of seconds are conceivable and promise to reach energy scales up to 300 TeV (ACME III project), well beyond the direct reach of the LHC or any other near- or medium-term particle collider. In this respect RbSr is a template rather than a target: the molecule RaAg, proposed for eEDM searches with an effective internal field of 65 GV/cm [17], is likewise built from an alkaline-earth atom and an electronegative, alkali-like partner and shares the same $^2\Sigma$ ground state, so that the association and transfer techniques developed for RbSr should pave the road.

Quantum chemistry and collisional shielding. Producing molecules in the ultracold regime opens the door to chemistry in a regime where a single partial wave and a single quantum state contribute, and where reactants, intermediates and products can be resolved in state and in time [18]. Understanding the reaction channels will help suppressing losses, which is the outstanding obstacle on the way to evaporative cooling of molecular samples [19]. By dressing RbSr molecules with a DC electric field ($E \approx 2.3$ kV/cm [6]) or with microwaves [20], the long-range van der Waals interaction between two molecules can be made repulsive, keeping the pair away from the short internuclear distances at which it would react.

1.3 Thesis overview

This thesis is organized in three additional chapters, followed by conclusions and outlook.

Chapter 2 introduces the experimental apparatus and the techniques used to produce an ultracold ^{87}Rb–^{87}Sr mixture. After a description of the vacuum system, the dual-species oven and the magnetic field coils, I review the relevant transitions of Rb and of Sr and the laser systems that address them. A section discusses the physics of the mixture: the role of the interspecies scattering length in thermalization, three-body losses and molecule formation, the universal relation between scattering length and binding energy of the least bound state, and the reason why ^{87}Rb–^{87}Sr is at the same time the most promising and the most fragile isotopic combination available. The chapter closes with a description of the experimental sequence, which is long and involved because ^{87}Rb and ^{87}Sr cannot be cooled together and must be prepared in separate dipole traps and merged only at the very end. This chapter is also meant as an entry point for students joining the experiment.

Chapter 3 is dedicated to the one-dimensional (1D) optical lattice. It begins with the theory of optical dipole traps and of the standing-wave potential obtained by retro-reflecting a focused beam, and continues with the two independent methods we use to calibrate the lattice depth on the atoms: parametric heating, which measures the resonant response of atoms trapped in an harmonic potential, and Kapitza-Dirac diffraction of a Rb BEC, which allows us to estimate the depth of the lattice from coherent oscillation between Bloch bands. Both methods returned lattice frequencies well below the calculated ones, and a big part of the chapter describes the methods with which we found the source of this large discrepancy. Only by directly looking

at the interference pattern we could say that the problem was the coherence of the light. A beatnote measurement of the phase noise identified a broadband noise background in the fiber amplifier as the culprit. Replacing the amplifier restored the expected lattice frequencies. The chapter ends with the motivation for the lattice: the confinement-induced stabilization of a resonantly interacting mixture, which we demonstrate experimentally, and the prospect of a confinement-induced resonance as an alternative to magnetoassociation.

Chapter 4 presents the photoassociation work. After an introduction to one- and two-photon photoassociation spectroscopy, I describe the optical setup I built during my project. The setup includes an injection-locked laser seeded with 689 nm light, whose injection bandwidth I characterized as a function of diode temperature and seed power, followed by two double-pass acousto-optic modulators that generate the free-bound and bound-bound frequencies. I then report the one-photon spectroscopy results, first on the simpler ^{87}Rb–^{88}Sr mixture, where four known lines are reproduced and found to be narrower than in previous measurements, and then on ^{87}Rb–^{87}Sr, where the target line is measured both in three dimensions and in the quasi-two-dimensional geometry provided by the lattice. The chapter closes with a description of the planned next steps: two-photon spectroscopy, a second lattice beam, and coherent transfer of the population into the electronic ground state by stimulated Raman adiabatic passage.

Chapter 5 summarizes the results and outlines the outlook of the experiment.

Chapter 2

Experimental setup and methods

The RbSr experiment at the Van der Waals-Zeeman Institute at the Univesiteit van Amsterdam aims to the first sample of ultracold dimers of an alkali and an earth-alkali atoms, rubidium and strontium respectively. Construction of the core of the apparatus began in 2006, with the initial objective of producing the first degenerate quantum gases of Sr. Between 2009 and 2010, the first Bose–Einstein condensates (BECs) of ^{84}Sr [21] and ^{86}Sr [22], as well as the first degenerate Fermi gas of ^{87}Sr [23], were obtained. Starting in 2012, the setup was upgraded to realize ultracold Rb–Sr mixtures and subsequently succeeded in generating doubly-degenerate gas mixtures of Sr and Rb [9].

This chapter gives a brief overview of the experimental apparatus and techniques, beginning with the dual-species oven and the vacuum system. The second and third sections are devoted, respectively, to rubidium and strontium transitions and their associated laser systems. In the fourth section, the main properties of an ultracold mixture of these two elements are examined. The final section outlines the experimental sequence required to obtain such an ultracold mixture and to pursue molecule formation.

The purpose of this chapter is to serve as an introduction for new Bachelor's, Master's, and PhD students who are encountering the experiment for the first time. For more detailed descriptions of the setup, see [24] for the vacuum chamber and Sr subsystem and [9] for the Rb subsystem.

2.1 The machine

The vacuum vessel consists of two main sections: the oven section and the science section. The pressure in the oven section is approximately 10^{-8} mbar, and it is connected to a differential pumping tube that enables pressures on the order of 10^{-11} mbar in the science section. A gate valve allows for independent venting and replacement of the rubidium and strontium reservoirs when they are depleted, without compromising the UHV conditions in the science region (fig. 2.1).

Oven section. A multi-species oven produces a collimated atomic beam directed along the machine axis. The oven is a linear stack of individual reservoirs containing

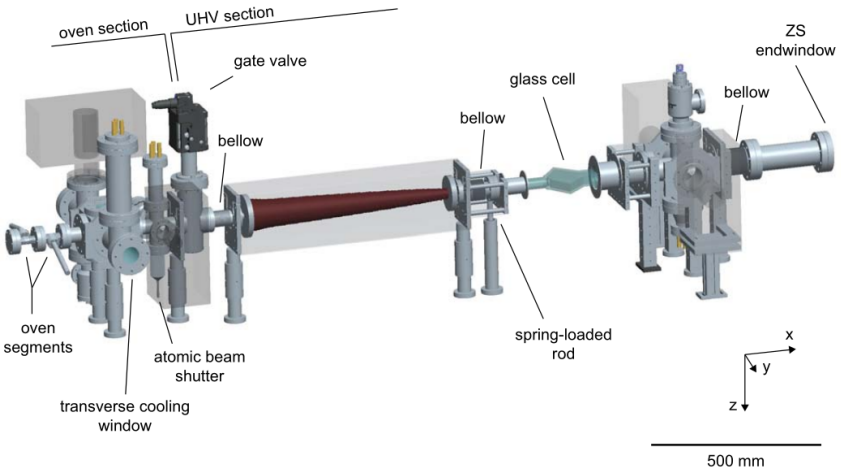


Figure 2.1: Technical drawing of the vacuum system. From [24].

samples of the two elements. Rubidium is heated up to 100 °C while Strontium to 500 °C. The atomic beam traverses two successive differential pumping stages separated by a six-way CF 40 cross. Ion pumps and Ti:Sub pumps maintain the pressure gradient. A motorized beam shutter blocks the atomic flux during sensitive experimental phases. Strontium depositing on the chamber walls acts as an additional getter, improving the vacuum quality in the oven .

UHV section. The UHV section begins with a Zeeman slower of approximately 60 cm length and 14 mm inner bore diameter, which simultaneously serves as a differential pumping stage. The slower is water-cooled from the inside. It connects via a welded bellow to a rectangular glass cell. The window on the opposite side, in front of the Zeeman-slower, is made of sapphire and heated to 150 °C to suppress Sr deposition. Two ion pumps and a Ti:Sub pump are attached to the cross at the back of the cell. The vacuum lifetime, assessed via the decay of magnetically trapped $^3P_2$ atoms, is approximately 30 s (limited by black-body induced decay from the metastable state itself); the lifetime of atoms in an optical dipole trap exceeds 2 minutes.

Magnetic Field Coils. The coil system around the glass cell can reach fields up to 1500 G with a precision of $\sim$ 1 mG. The core of the system consists of two pairs of coils in near-Helmholtz configuration: the *Feshbach coils* (up to $\sim$600 G in Helmholtz and $\sim$100 G/cm in anti-Helmholtz configuration) and the *Curvature coils* (up to $\sim$400 G), both wound from $4 \times 4\,\mathrm{mm}^2$ square copper wire with a $2 \times 2\,\mathrm{mm}^2$ water-cooled bore. Fast switching is provided by *Fast coils* (6 windings) and *Anti-Curvature coils* (5 windings) through mechanical relays.

Static external fields ($\sim$500 mG total from the Earth's field and ion pump stray fields) are compensated at the atoms' position by a set coils wound onto a cubic frame of $\approx 1\,\mathrm{m}^3$ surrounding the chamber. Time-varying stray fields fluctuations of a few mG in the horizontal plane are particularly harmful during red-MOT loading [25] (a 3 mG field change displaces the MOT by $\sim$50 μm).

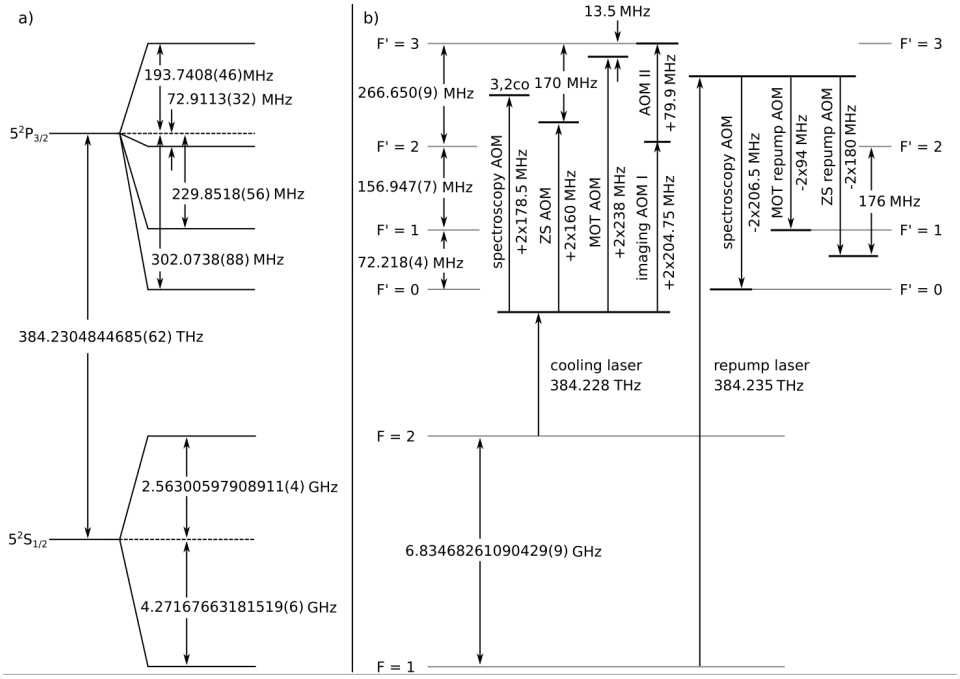


Figure 2.2: a) Hyperfine structure of the ^{87}Rb D_2 line [28] and b) laser system detunings. Figure from [9].

2.2 Rb Setup

Rubidium is an alkali element (group I) with groundstate electronic configuration $[\mathrm{Kr}]\,5s^1$, featuring one valence electron in the outer s-shell. Its level structure is analogous to Hydrogen and it has two stable isotopes: ^{87}Rb has a s-wave scattering length of $\approx 100\,a_0$ ($a_0 = 0.529177210\,\text{Å}$), which made it one of the first elements to be laser cooled and to reach quantum degeneracy. The other stable isotope is ^{85}Rb but it exhibits a large negative scattering length at low magnetic fields. Feshbach resonances are accessible by the use of a magnetic field [26], but this would add complexity to the experiment. For this reason, we use ^{87}Rb.

Energy levels. Laser cooling of ^{87}Rb is performed on the $5s\,^2S_{1/2} \rightarrow 5p\,^2P_{3/2}$ transition at 780 nm. The magneto-optical trap (MOT), Zeeman slower (ZS) and imaging light addresses the $(F = 2) \rightarrow (F' = 3)$ hyperfine transition. Off-resonant excitation to $(F' = 2)$, however, allows decay into the dark $(F = 1)$ ground state, so continuous repumping on the $(F = 1) \rightarrow (F' = 2 \text{ or } 1)$ transitions is required to sustain cycling and to image $(F = 1)$ atoms.

We make use of dipole traps at 1064 nm and Rb polarizability at this wavelength is $687\,a_0^3$ [27].

Laser system. Cooling and repumper lights are generated by two separate external cavity diode lasers (ECDLs) (Toptica TA-pro), each one of them locked to a Rb vapour cell through modulation-transfer spectroscopy, with AOMs used downstream to generate the individual MOT, ZS, and imaging beams at the required detunings. The cooling laser is locked to the $(F = 2) \rightarrow (F' = 3, 2_{\mathrm{co}})$ crossover resonance and

produces 900 mW, sufficient for the ∼25 mW per MOT beam and ∼75 mW ZS optical paths. The repumper laser is locked to the $(F = 1) \rightarrow (F' = 0)$ line its output gets distributed to the spectroscopy cell (200 μW), the ZS (5 mW), and two MOT repumper beams of several 100 μW each (resonant with $(F = 1) \rightarrow (F' = 1)$). All beams are delivered to the vacuum assembly via polarization-maintaining optical fiber.

One of the two MOT repumper beams is used for standard optical pumping during loading and imaging; the other, a "dark-spot" beam, is used only during dipole trap loading. A wire placed near the glass cell casts a shadow into this beam, overlapped with the storage optical dipole trap (ODT), so that atoms within the ODT are pumped into the dark $(F = 1)$ state and no longer scatter resonant light. This dark-spot technique increases the achievable atomic density in the ODT.

The dipole trap is obtained by focusing 30 W from a 100 W fiber laser at 1070 nm (YLR-100-LP-AC-Y12 from IPG). The beam waist at the focus is around 86 μm with a Rayleigh range of 5 cm.

2.3 Sr setup

Strontium is an alkaline-earth element (group II) with groundstate electronic configuration [Kr] $5s^2$, featuring two valence electrons in the outer s-shell. Its level structure is analogous to that of helium, with singlet and triplet manifolds connected by narrow intercombination transitions. These properties make Sr particularly attractive for laser cooling and quantum gas experiments, and have established it as a leading platform for optical lattice clocks [29].

Strontium has four naturally occurring isotopes. The three bosonic isotopes, ^{84}Sr (0.56%), ^{86}Sr (9.86%) and ^{88}Sr (82.60%), have zero nuclear spin, a consequence of the paired-nucleon structure of even-even nuclei. The single fermionic isotope, ^{87}Sr (7.00%), carries nuclear spin $I = 9/2$, the largest of all stable alkaline-earth isotopes. The higher number of levels of the fermionic isotope makes all the laser cooling stages more complex and less efficient with respect to its bosonic counterparts. Here I will briefly describe the cooling transitions valid for the bosonic isotopes, while a discussion of fermionic cooling schemes can be found in [24].

2.3.1 Sr level scheme

The broad $^1S_0 \rightarrow {}^1P_1$ transition at $\lambda = 461$ nm has a natural linewidth $\Gamma_{\text{blue}} = 2\pi \times 30.5$ MHz [30]. The high scattering rate of this transition makes it very effective for transverse cooling, Zeeman slowing and the first MOT. We refer to it as the *blue* transition.

The $^3P_0$, $^3P_1$, and $^3P_2$ states are nominally stable against single-photon decay to the $^1S_0$ ground state, as it would require an electron spin flip. They acquire finite lifetimes through higher-order processes. In our experiment we make use of the $^1S_0 \rightarrow {}^3P_1$ transition, in which a spin-orbit mixing of $^1P_1$ character enables a weak E1 transition to the ground state, resulting in $\tau(^3P_1) = 21.4\,\mu$s [30]. The corresponding linewidth of $\Gamma_{\text{red}} = 2\pi \times 7.4$ kHz, makes this transition extremely useful for second-stage narrow-line MOT. Temperatures as low as hundreds of nK can be achieved, since the Doppler temperature $T_D = \hbar\Gamma/2k_B = 179$ nK is smaller

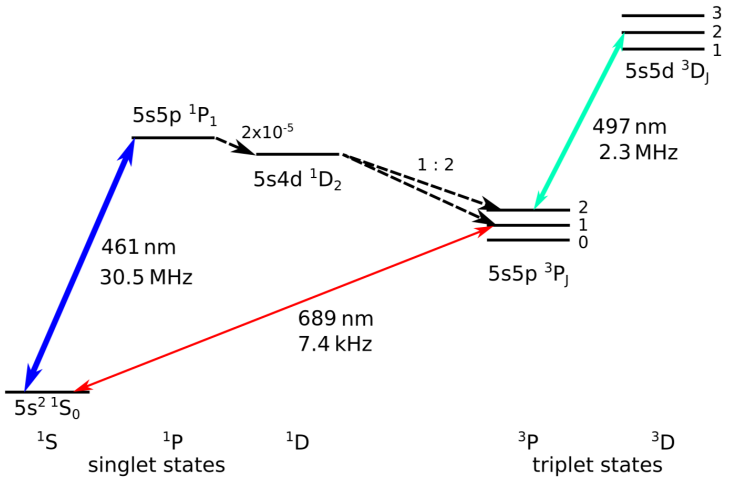


Figure 2.3: Bosonic Sr level scheme from [9]. Just the three transitions used in the RbSr experiment are highlighted. For the fermionic isotope scheme has many more levels due to the non zero nuclear spin $I = 9/2$.

than the recoil temperature $T_r = \hbar^2 k^2 / k_B m = 460\,\text{nK}$. We refer to it as the *red* transition.

The nonzero branching ratio between the $^1P_1$ and the $^1D_2$ states opens a decay channel from blue MOT cycle. This branching ratio is roughly $1 : 50\,000$. The atoms decay further into the $^3P_1$ and $^3P_2$ metastable triplet states with a branching ratio of $2 : 1$. Atoms in the $^3P_1$ state have a lifetime of only $21\,\mu\text{s}$ before they decay back into the $^1S_0$ state. On the other hand, the $^3P_2$ state has a lifetime of 500 s. In order to pump these atoms back to the ground state, an additional transition has to be used. Among the many possible options [24], we make use of the $^3P_2 \rightarrow 5s5d\,^3D_2$ transition, addressed by a laser at 497 nm. On average three photon are scattered before the atoms decay to the $^3P_1$ state. We refer to it as the *green* transition.

The isotope shifts of the relevant transitions are given in tab. 2.1, referenced to ^{88}Sr. The shifts are on the order of 100 MHz for the blue and red transitions, easily within reach via acousto-optical modulators (AOMs).

Isotope	$^1S_0 \rightarrow {}^1P_1$	$^1S_0 \rightarrow {}^3P_1$	$^3P_2 \rightarrow 5s5d\,^3D_2$
^{84}Sr	−270.8	−351.5	−91.8
^{86}Sr	−124.8	−163.8	−47.5
^{87}Sr	−46.5	−62.2	–
^{88}Sr	0	0	0

Table 2.1: Isotope shifts in MHz of the $^1S_0 \rightarrow {}^1P_1$ and $^1S_0 \rightarrow {}^3P_1$ transitions, referenced to ^{88}Sr [31].

The fermionic isotope ^{87}Sr ($I = 9/2$) has only one hyperfine state in the $^1S_0(F = I = 9/2)$ manifold. The $^1P_1$ hyperfine structure is composed by three states but the separation is of the same order of magnitude of the linewidth. The $^3P_1$ hyperfine structure is well resolved and is summarized in tab.2.2. Contrarily to Rb, the g_F factors of the $^3P_1$ states are much larger than those of the $^1S_0$ state (which arise purely from the nuclear magnetic moment), giving rise to complex red MOT dynamics.

F	${}^1S_0 - {}^1P_1$	${}^1S_0 - {}^3P_1$	${}^3P_2 \to 5s5d\,{}^3D_2$
7/2	+37	+1414.12	+536
9/2	−23	+283.86	+214
11/2	−6	−1179.29	−179
13/2	–	–	−644

Table 2.2: Selected hyperfine splittings in MHz of ^{87}Sr main transitions, referenced to a fictitious $^{87}\mathrm{Sr}(I = 0)$ state. To get the absolute frequency one has to start from ^{88}Sr transition frequency and then add the isotope shift and the offsets.

Similarly to Rb, we load Sr in dipole traps at 1064 nm. Its polarizability at this wavelength is $240\,a_0^3$ [32].

2.3.2 Sr laser system

Blue. The 461 nm light was originally obtained by doubling IR light, but the advent of blue laser diodes made possible to shift to a more handy external cavity diode laser (ECDL) laser. Since the linewidth of the transition is 30 MHz, the short term stability of the ECDL itself is good enough. Long term stability is achieved trough locking to a spectroscopy cell on the $^{88}\mathrm{Sr}\ {}^1S_0 \to {}^1P_1$ transition by modulation transfer spectroscopy.

A master ECDL provides 40 mW of light. Few mW are sent to the spectroscopy while the rest is injected into two other 461 nm injection locked lasers (ILL). One ILL provides 25 mW for the transverse cooling stage of Sr right after the oven, while the other ILL provides 200 mW for the Zeeman-slower, the MOT and the imaging system. To quickly switch between different isotopes a double pass AOM right before the spectroscopy cell shifts the locking point. A set of AOMs makes it possible to choose the optimal detunings.

Green. The green repumper laser at 497 nm is a Toptica SHG system, consisting of a 994 nm diode laser that is doubled in a LBO crystal in a bowtie cavity. The output power of the IR diode is 300 mW and the second harmonic power is 25 mW. A set of AOMs offer a large tuning range of more than a GHz if used in series or to address all the necessary transitions for the current isotopic combination if used in parallel. Frequency stability is obtained by locking the IR light to an ultra-low expansion (ULE) reference cavity. One of the cavity mirrors is mounted on a piezo-actuator. The cavity length can be tuned by an applied high voltage to adjust the laser frequency. The cavity drift is of the order of 10 MHz per day, which means that once a day the cavity offset has to be optimized on atoms by directly observing its influence on a live blue MOT.

Red. The 689 nm laser system, addressing the ${}^1S_0 \to {}^3P_1$ intercombination transition, is the most complex laser system in the apparatus: the transition's natural linewidth of 7.4 kHz requires the laser linewidth to be actively stabilized, In addition, all isotope shifts and hyperfine components, spanning up to a few GHz, have to be reached.

The master laser is a Toptica DLpro (intrinsic linewidth $\sim$1 MHz), narrowed by locking to a high-finesse ($\approx$ 15 000) Pound-Drever-Hall reference cavity via a

Toptica FALC servo, after passing through a mode-cleaning fiber. The resulting linewidth, estimated from the lock error signal, is $\lesssim 2\,\mathrm{kHz}$. The cavity itself is housed in a thermally and acoustically shielded wooden box but lacks active temperature stabilization.

Long-term stability is achieved by locking the cavity to a home-built Doppler-free frequency modulation spectroscopy cell, locked to the ^{88}Sr peak, since it is the most abundant isotope and allows to have the strongest signal. The light is shifted by an 80 MHz AOM. A loudspeaker magnet provides an inhomogeneous field that spreads out the $m_J = \pm 1$ Zeeman components, isolating the $\Delta m_F = 0$ feature. The AOM is frequency-modulated at $\pm 10\,\mathrm{kHz}$, and the resulting lock-in signal drives a slow PID (time constant of tens of seconds) acting on the cavity piezo.

All required frequencies for the red MOTs are derived directly from the master laser via a cascade of AOMs on a breadboard called "red spider" from the large number of black fibers that are connected to it. The system also supplies light for other purposes like the optical Stern-Gerlach (OSG) experiment and photoassociation (PA) spectroscopy.

Each red-spider output carries only few hundreds of μW, which is not sufficient. Amplification is achieved by injection locking three Toptica DL100 lasers with the red-spider light. The ILL outputs are combined on non-polarizing 50:50 beamsplitters into four ports: three drive the MOT axes (via individual AOMs and shutters), and the fourth is split for red-transition imaging and for monitoring all ILLs on a shared Fabry-Pérot (FP) cavity.

Dipole traps. We employ a total of five dipole trap beams derived from 3 different high-power laser sources. Because of the anomalously large inter-species scattering length of ^{87}Rb and ^{87}Sr (see section 2.4), the two species must be initially loaded into two separate horizontal dipole traps. A third dipole trap is arranged so that it crosses both of these traps vertically, almost at right angle. This configuration confines the atoms along the axial direction and guarantees spatial overlap of the atomic clouds once the traps are merged (see section 2.5). All high-power beams pass through AOMs, allowing their intensities to be controlled independently of one another.

A 100 W laser (YLR-100-LP-AC-Y12 from IPG) at 1070 nm is split in three parts. About 35 W are used for the *reservoir trap*, where ^{87}Rb and ^{88}Sr are loaded after the MOT stages. Another 15 W are used for the *lower-static trap*, in which we load ^{87}Sr. About 1 W is used for the *connecting dimple* beam, the dipole trap which purpose is to connect the reservoir and the lower traps. It is worth noting that this laser source has very short coherence length and therefore we do not expect any interference arising from the overlap of the beams.

A 50 W fiber laser (Azur Light Systems, ALS-IR-1064-50-E-CC-SF) at 1064 nm is used for the *lower-dynamic trap* (10 W). Once ^{87}Sr is cold, it gets loaded into the overlap of the lower-static and lower-dynamic traps. After the evaporation stage, a mirror with two piezoelectric transducers lifts the lower-dynamic trap such that it moves upward and overlaps with the reservoir trap.

The last high power source is a 15 W amplifier (NKT Boostik) at 1064 nm, seeded with about 20 mW of light coming from a Mephisto MOPA (master oscillator-power amplifier). A maximum of 5 W are aligned to overlap with the reservoir trap and

almost parallel to it. A mirror retroreflects the beam to create an optical lattice (see Chapter 3).

2.4 Rb–Sr ultracold mixture

Ultracold quantum mixtures provide a versatile platform for investigating a broad range of few-body and many-body phenomena [1] and are the starting point for photoassociated molecules. The constituents can be chosen from any combination of quantum statistics, realizing Bose-Bose (BB), Fermi-Fermi (FF), or Bose-Fermi (BF) mixtures, each exhibiting qualitatively distinct physics governed by the interplay between intra- and inter-components interactions, and mass ratios. In heteronuclear mixtures, the two species interact via an interspecies s-wave scattering length a_{12}, which can in principle be tuned via interspecies Feshbach resonances (FR) [33].

The ^{87}Rb –^{87}Sr mixture studied in this work is a BF system in which ^{87}Rb is bosonic and ^{87}Sr is fermionic. The two species differ in mass by approximately $\Delta m/m \leq 0.01$, making this a nearly mass-balanced BF mixture.

Although FR between Rb and Sr have been predicted [7] and observed [8] up to few kG, they are only few mG wide due to the non magnetic nature of closed shell atoms like Sr. This makes it technically very challenging to use FR to tune a_{12} and produce molecules. On the other hand, an advantage of working with alkaline-earth species is the relatively high abundance of stable isotopes. Strontium has four and this feature gives more freedom of choice when considering effective thermalization and molecules formation.

s-wave scattering length

In the ultracold regime, the scattering amplitude becomes isotropic and energy-independent, as long as the collision energy satisfies $E_k \ll \hbar^2/(2\mu a_c^2)$, where μ is the reduced mass and a_c is the characteristic length of the interaction potential [34]. All partial waves with $\ell > 0$ are suppressed by the centrifugal barrier, and scattering is entirely determined by the s-wave phase shift $\delta_0(k)$, which vanishes linearly with k as $k \to 0$. The entire two-body interaction is therefore encoded in a single parameter, the s-wave scattering length:

$$a = -\lim_{k\to 0} \frac{\tan \delta_0(k)}{k}. \tag{2.1}$$

Crucially, this quantity does not depend on the details of the short-range potential: two potentials with identical scattering lengths produce the same low-energy scattering cross section $\sigma = 8\pi a^2$ (for identical bosons) and, in the dilute limit $n|a|^3 \ll 1$, the same macroscopic many-body properties. The sign and magnitude of a determine the mean-field interaction energy $U = 4\pi\hbar^2 an/m_{\text{atom}}$ felt by a distinguishable particle traversing a medium of spatial density n: positive a corresponds to effective repulsion, negative a to attraction.

In the context of a heteronuclear mixture such as Rb–Sr, the interspecies scattering length a_{12} governs two distinct but related physical processes. The first is thermalization. Elastic interspecies collisions redistribute energy between the two components, which is essential both for sympathetic and evaporative cooling. A

small interspecies scattering length makes thermalization inefficient. On the other hand, a large positive scattering length also enhances the three-body recombination rate, which scales as $K_3 \propto a_{12}^4$, causing inelastic loss and heating that compete directly with molecule association and limit the lifetime of the mixture. Finally, a negative scattering length favors inelastic precesses that lead to a collapse of the cloud. In general, a scattering length that is a good compromise between efficient thermalization and low losses is around $100\,a_0$.

The second role of a_{12} concerns molecule formation (see paragraph *Molecules formation)*, since the value of the scattering length and the energy of the least bound state are not independent quantities.

-	^{87}Rb	^{88}Sr	^{87}Sr
^{87}Rb	100.4	170.3	1421
^{88}Sr	170.3	-1	55
^{87}Sr	1421	55	97

Table 2.3: Rb–Sr inter- and intra-species s-wave scattering lengths for the combinations of isotopes used in our experiment. Values are in units of the Bohr radius a_0 [35, 24, 6].

Sympathetic and evaporative cooling

Most ultracold atom experiments rely on laser cooling followed by evaporative cooling to reach quantum degeneracy. The latter process intrinsically leads to a loss of atoms. To minimize this loss, it is beneficial to develop laser cooling methods that are able to reach high phase space densities (PSDs). The main atomic transition for laser cooling of alkalies, such as Rb, is broad, on the order of several MHz. To achieve high PSDs by laser cooling of such species, one can apply sub-Doppler cooling techniques, such as polarization gradient cooling in optical molasses. As a member of the alkaline-earth family, Sr has a singlet/triplet electronic structure. Its $^1S_0 \rightarrow {}^3P_1$ intercombination line has a width of only 7.4 kHz. With simple Doppler cooling using this narrow line, one can reach temperatures as low as few hundreds of nK. It is therefore tempting to transfer those excellent properties to other species, by using Sr as a cooling agent.

By choosing the Sr isotope with a good scattering length with Rb, thermalization is efficient and the sympathetic cooling technique can be used. The ^{87}Rb–^{88}Sr mixture has inter-species s-wave scattering length of $170\,a_0$ 2.3 which provides a better elastic to inelastic collision rate. Rb thermalizes with Sr in the optical trap and gets cooled down to few μK.

Another important factor is the different polarizabilities at 1064 nm. Rubidium is ≈ 2.9 times more trapped than Sr, which makes it possible to evaporate completely strontium while keeping a big fraction of nearly degenerate Rb atoms. By lowering even more the trap depth also Rb atoms evaporate, and a BEC of 2×10^4 atoms cam be achieved in our RbSr setup.

Molecules formation

The size and binding energy of the last two-body bound state below a collision threshold are not independent quantities: in the regime where the scattering length

a is large compared to the characteristic range of the interaction, the near-threshold physics becomes *universal*, *i.e.* independent of the short-range details of the potential and controlled by a alone [33]. For such large scattering lengths, the last vibrational level of the interaction potential is a shallow "halo" state with binding energy well approximated by

$$E_b = \frac{\hbar^2}{2\mu a^2}\,. \tag{2.2}$$

Equation (2.2) makes the intuition quantitative: since $E_b \propto 1/a^2$, an *increase* in the scattering length necessarily corresponds to a bound state *closer* to the scattering continuum.

For the isotopologue used in this work, ^{87}Rb–^{87}Sr, the reduced mass is $\mu = m_{\mathrm{Rb}} m_{\mathrm{Sr}}/(m_{\mathrm{Rb}} + m_{\mathrm{Sr}}) = 43.45\,\mathrm{u}$ — essentially $\mu \simeq m/2$, since ^{87}Rb and ^{87}Sr happen to share the same mass number. considering the large background scattering length $a = 1421\,a_0$, Eq. (2.2) gives

$$E_b = h \times 20.5\,\mathrm{kHz}\ \ (\simeq k_B \times 1.0\,\mu\mathrm{K})\,, \tag{2.3}$$

i.e. a molecular state only a few tens of kHz below the two-atom threshold.

Such a shallow binding energy makes an alternative route attractive: because $E_b/h = 20.5\,\mathrm{kHz}$ is comparable to trap frequencies routinely produced in an optical lattice, the near-threshold RbSr pair state might instead be accessed through confinement-induced resonances (CIRs)[36, 11].

2.5 Experimental sequence

In this section I report the main steps of the experimental sequence. As we saw in the previous section 2.4, many physical and technical constraints have to be taken into account, making the sequence long and complex.

The same Zeeman slower (ZS) is used to slow both atomic species. Since the magnetic fields required to slow Rb and Sr differ significantly, we perform a time sequential loading scheme. We first perform the Rb MOT and load it into a dipole trap, and then the Sr MOTs and load them into two dipole traps. Due to the huge scattering length and the associated strong three-body losses between ^{87}Rb and ^{87}Sr, we cannot load them into the same trap. Nevertheless, by choosing the ^{88}Sr isotope, we can still exploit its narrow linewidth cooling transition to sympathetically cool Rb to $1.5\,\mu$K level. For these reasons ^{87}Sr is loaded in a trap about $300\,\mu$m lower than the reservoir trap, where Rb and ^{88}Sr are trapped. The mixture of interest is obtained later in the sequence by moving the lower trap and overlapping it with the reservoir-dimple cross dipole trap.

The resulting experimental sequence is very long, up to almost one minute. The sequence is produced by a control system[1] that relies on a parallel bus distributing data from a central computer to analog, digital, and radio-frequency output boards. This bus operates at 2 MHz and can address up to 4096 devices, each 16 bits wide. The software component consists of two parts: a C++ control program running on the computer connected to the output hardware, and a data acquisition program running on the computer to which a camera is attached, used to record the results of each experimental run.

[1] See the SrBEC/Control System website: `https://www.strontiumbec.com/`

2.5.1 Rb cooling sequence

The Zeeman slower beam carries 14 mW of power detuned by −165 MHz from the $(F = 2) \rightarrow (F' = 3)$ transition, overlapped with a 4.5 mW repump beam resonant with $(F = 1) \rightarrow (F' = 1)$. Slowed atoms are captured in a 3D MOT with beams of 9.8 mm waist, 18 mW (25 mW) power in the horizontal (vertical) direction, detuned by −16 MHz from the $(F = 2) \rightarrow (F' = 3)$ transition. The repumper beam has a waist of 6 mm and 130 μW/cm^2 peak intensity, resonant with $(F = 1) \rightarrow (F' = 2)$, and is overlapped with the MOT. The quadrupole field gradient is 12 G/cm along the vertical axis.

The MOT is loaded for 700 ms, accumulating almost 10^7 atoms. The cloud is then compressed in 140 ms by increasing the quadrupole gradient to 50 G/cm and the laser detuning to −30 MHz, reducing the cloud radius to ∼250 μm. A short polarization gradient cooling stage follows: the quadrupole field is switched off, the detuning is set to −110 MHz, and the beam power is halved. After 3 ms of optical molasses, 8×10^6 atoms remain at 20 μK.

The atoms are then loaded into the reservoir dipole trap formed by an horizontal reservoir beam (86 μm waist, power 35 W) crossing the dimple beam (53 μm waist, power 1 W). The beam is linearly polarized along the vertical direction to minimize the differential light shift on the Sr red cooling transition. Loading is assisted by a dark-spot repumper beam in which a wire is imaged onto the trap region, preventing repumping of atoms already captured in the trap. With the repumper intensity reduced to 8 μW/cm^2, we transfer up to 3×10^6 atoms at a density of 2×10^{13} cm^{-3} and a temperature of ∼20 μK in 500 ms.

2.5.2 Sr cooling sequence

Blue MOT and metastable reservoir. Sr vapor at ∼ 500°C is emitted from the oven. Transverse cooling with light detuned by $\approx \Gamma/2$ from the $^1S_0 \rightarrow {}^1P_1$ transition reduces the beam divergence and increases the MOT loading rate by up to a factor of three. The Zeeman slower decelerates the beam prior to capture.

In the MOT region, three retroreflected beams at 461 nm illuminate the atoms with intensities $I_{\mathrm{vert}} \approx 0.1\, I_{\mathrm{sat}}$ and $I_{\mathrm{hor}} \approx 0.25\, I_{\mathrm{sat}}$, at a detuning of $\Delta = -1.0\,\Gamma \approx -32$ MHz and a quadrupole field gradient of 55 G/cm along the vertical direction. The resulting Doppler temperature is $T_D = \hbar\Gamma/2k_B = 720\,\mu$K, well above the recoil temperature $T_r = \hbar^2k^2/mk_B = 1.04\,\mu$K.

Atoms in the $^1P_1$ state decay with a branching ratio of approximately 1 : 50 000 into the $5s4d\,{}^1D_2$ level, and further into the $^3P_1$ and $^3P_2$ metastable states in a 1 : 2 ratio. Atoms in the $^3P_1$ state return to the ground state within 21 μs, while those in weak-field-seeking m_F substates of $^3P_2$ are trapped by the MOT quadrupole field. This *metastable reservoir* accumulates 10^7–10^8 ^{88}Sr atoms over loading times of 50 ms to 10 s depending on isotopic abundance, and has a lifetime of approximately 30 s in our apparatus, limited by black-body radiation.

Once ^{88}Sr is trapped in the metastable state, the slowing and the blue MOT for ^{87}Sr take place, and atoms are accumulated in the metastable reservoir. The same procedure as for the bosonic isotope is followed, but the presence of the hyperfine structure makes it less efficient.

Atoms are optically pumped back from the $^3P_2$ metastable reservoir into the

ground state via the repump laser at 497 nm, driving the $^3P_2 \to 5s5d\,^3D_2$ transition. From the $^3D_2$ state, atoms decay preferentially into the $^3P_1$ state (branching ratio 2 : 1 relative to $^3P_2$), and subsequently return to $^1S_0$ within 21 μs. The repumper pulse lasts 50 ms.

Narrow-line red MOT. Since the atoms emerge from the metastable reservoir at temperatures ~ 1 mK, a single laser frequency at the red MOT $^1S_0 \to {}^3P_1$ transition cannot provide sufficient capture efficiency. We therefore apply a frequency-broadened MOT in the first capture phase: an AOM generates a frequency comb spanning from -200 kHz to -5 MHz detuning with a scan rate of ~ 20 kHz. The total power is $\sim 2000\, I_{\rm sat}$ and each comb tooth has $\sim 10\, I_{\rm sat}$. The capture phase lasts 50 ms with a MOT lifetime exceeding 1 s. In a second phase, the comb range is narrowed to 2 MHz and the intensity reduced to $\sim 100\, I_{\rm sat}$. Since the linewidth is narrow, we can spatially separate the ^{88}Sr from the ^{87}Sr by changing the detunings of the MOTs' beams.

Operation then switches to a single-frequency ^{88}Sr MOT at $\Delta = -800$ kHz, and the detuning and intensity are gradually ramped toward resonance. In the final single-frequency stage (~ 200 ms), conditions approach $|\Delta| \sim \Gamma_{\rm sat} \sim \Gamma$ and $s \to 1$, where the temperature approaches $T_r/2$. Typical final MOT conditions are $\sim 5 \times 10^6$ atoms at few μK for ^{88}Sr. We then load the MOT into a dipole trap (see next paragraph).

The narrow-line MOT of the fermionic isotope ^{87}Sr exhibits different dynamics due to the large ratio $g_e/g_g \gg 1$ between the $^3P_1$ and $^1S_0$ g-factors. In a conventional alkali MOT, the Zeeman shifts of ground and excited states are comparable, and all $m_F \to m_F \pm 1$ transitions share nearly the same resonance position. In ^{87}Sr, by contrast, the $^1S_0$ substates are nearly degenerate (nuclear g-factor only), so a light field at a given magnetic field can be simultaneously red-detuned for one m_F transition and blue-detuned for another. For some substates, the near-resonant beam expels the atom from the trap center; To prevent loss of atoms that enter non-resonant regions, a second *stirring* beam drives the $F = 9/2 \to F' = 9/2$ transition, overlapped with the trapping beam on the $F = 9/2 \to F' = 11/2$ transition. The stirring beam randomizes m_F states and broadens the resonance volume. Stable trapping arises only from the average over many absorption events, weighted by Clebsch-Gordan coefficients (see [24]). Final conditions of the fermionic red MOT are $\sim 2 \times 10^6$ atoms at few μK. The loading efficiency into the lower dipole trap is $\approx 30\%$.

Dipole trap loading. The ^{88}Sr cloud is overlapped with the crossing point of the reservoir and the dynamic dimple traps by shifting the quadrupole field center upward while keeping the red MOT detuned by -200 kHz. At this point the Sr density is low enough that its influence on the Rb cloud is negligible over 500 ms. The Sr cloud is then compressed by adjusting the quadrupole field, MOT detuning, and intensity simultaneously, loading Sr into the reservoir trap while keeping its position fixed. The light shift at the trap center is $\sim +500$ kHz (≈ 70 linewidths of the red transition), so to laser cool Sr inside the storage trap, the MOT frequency is ramped 350 kHz to the blue of the bare atomic resonance while the peak intensity is reduced to 6 μW/cm^2. Sr atoms not spatially overlapping with the dipole trap are

expelled, causing a 60% loss in Sr atom number. Given the high natural abundance of ^{88}Sr this loss is tolerated. The ^{88}Sr temperature after the compression is below $5\,\mu$K.

Once ^{88}Sr has been loaded in the trap, we perform the single frequency MOT for ^{87}Sr (see previous paragraph). Similarly to ^{87}Sr, the cloud is compressed and loaded into a dipole trap consisting in the intersection of the lower static, lower dynamic and the dimple beams.

At this stage we can decide to polarize the fermionic ^{87}Sr. We ramp a small bias field of 2 G and shine σ-polarized light coming from one of the red MOT $F = 9/2 \rightarrow F' = 9/2$ beams and sweep it through the m_F states ladder of the excited state. Depending on the polarization of the light we can pump the atoms to the $m_F = +9/2$ or $m_F = -9/2$. By exploiting the fact that $g_e/g_g \gg 1$ and the $(F = 9/2, m_F = \pm 9/2) \rightarrow (F' = 11/2, m_F = \pm 11/2)$ cyclic transitions driven by $\sigma_\pm$ light, we can spatially separate the $m_F = +9/2$ or $m_F = -9/2$ components. This separation by levitation method was developed by Simon Stellmer [23].

2.5.3 Sympathetic cooling and evaporation

The sympathetic cooling stage is central to our approach to a Rb–Sr ultracold mixture: we exploit Sr narrow-linewidth cooling to cool Rb and increase its phase-space density (PSD). While ^{88}Sr intraspecies scattering length is $-1\,a_0$, the inter-species scattering length with ^{87}Rb is $170\,a_0$, which allows for efficient thermalization. This feature also allows ^{88}Sr to thermalize through scattering with Rb and it has been essential in the past for reaching the Double BEC of ^{88}Sr and ^{87}Rb [9]. As Rb thermalizes with the laser-cooled Sr through elastic collisions, its PSD increases by more than a factor of 200, reaching 0.062(6) and a temperature of few μK, while little atoms are lost.

During the blue MOT stage, the magnetic field makes the high field seeking $m_F = +1$ component of Rb in $^2S_{1/2}(F = 1)$to leave the reservoir trap. In order to reestablish a uniform population distribution among the three m_F states, we apply microwave pulses resonant with the Zeeman splitting at a given magnetic field. Crucially, this process must not be a coherent process, otherwise populations undergo Rabi oscillations between the m_F states.

At the wavelength (1070 nm) of the dipole traps the polarizability of Rb is 2.9 times that of Sr, so the initial trap depths are $k_B \times 25\,\mu$K for Rb and $k_B \times 7\,\mu$K for Sr. This detail is of critical importance as it allows us to evaporate only Sr without losing much Rb by simply decreasing the reservoir trap depth. We decrease the trap depth to $k_B \times 10\,\mu$K for Rb in around 7 s and about 3×10^4 Rb atoms survive. This trick has been used also in the creation of the Double BEC of ^{84}Sr and ^{87}Rb [9] since evaporation with ^{88}Sr is preferred to ^{84}Sr due to isotopic abundances. By decreasing the trap depth even more we can produce a Rb BEC of 2×10^4 atoms, which we can use for characterizing the optical lattice by Kapitza-Dirac diffraction technique (see section 3.3.2).

At the same time we evaporate ^{87}Sr by decreasing the intensity of the lower static trap. due to the fact that we previously polarize the sample the thermalization process is not very efficient. We obtain 3×10^4 atoms at 400 nK.

2.5.4 Creation of the mixture and photoassociation

As mentioned before, ^{87}Rb and ^{87}Sr are kept separated during cooling and samples preparation stages due to the large 3-body losses that would otherwise heat up and deplete the mixture. At this point of the experimental sequence ^{87}Rb and ^{87}Sr are close to quantum degeneracy. All next steps have to be precisely tuned in order not to heat up the delicate samples, and this requires a lot of optimization.

To create the mixture we move the lower dynamic trap by mean of a mirror mounted on piezo actuators. By moving the beam such that it continuously crosses the dimple beam, the ^{87}Sr cloud remains confined in the intersection of the two. The ramp takes 200 ms.

At the same time, we ramp up an optical lattice on Rb, which is in the intersection of reservoir and dimple traps. We ramp the lattice before in order to avoid losses and heating at the moment of merging (see 3.1.1). we ramp the lattice to the value at which we have the strongest suppression of 3-body losses, around 45 kHz Rb lattice frequency.

Once the two atomic species are merged we can decide to ramp the lattice to different intensities to record for example its influence on the mixture lifetime (fig.3.1). The last step of the experiment consists in shining the PA beam on the mixture and measure the remaining population (see Chapter 4).

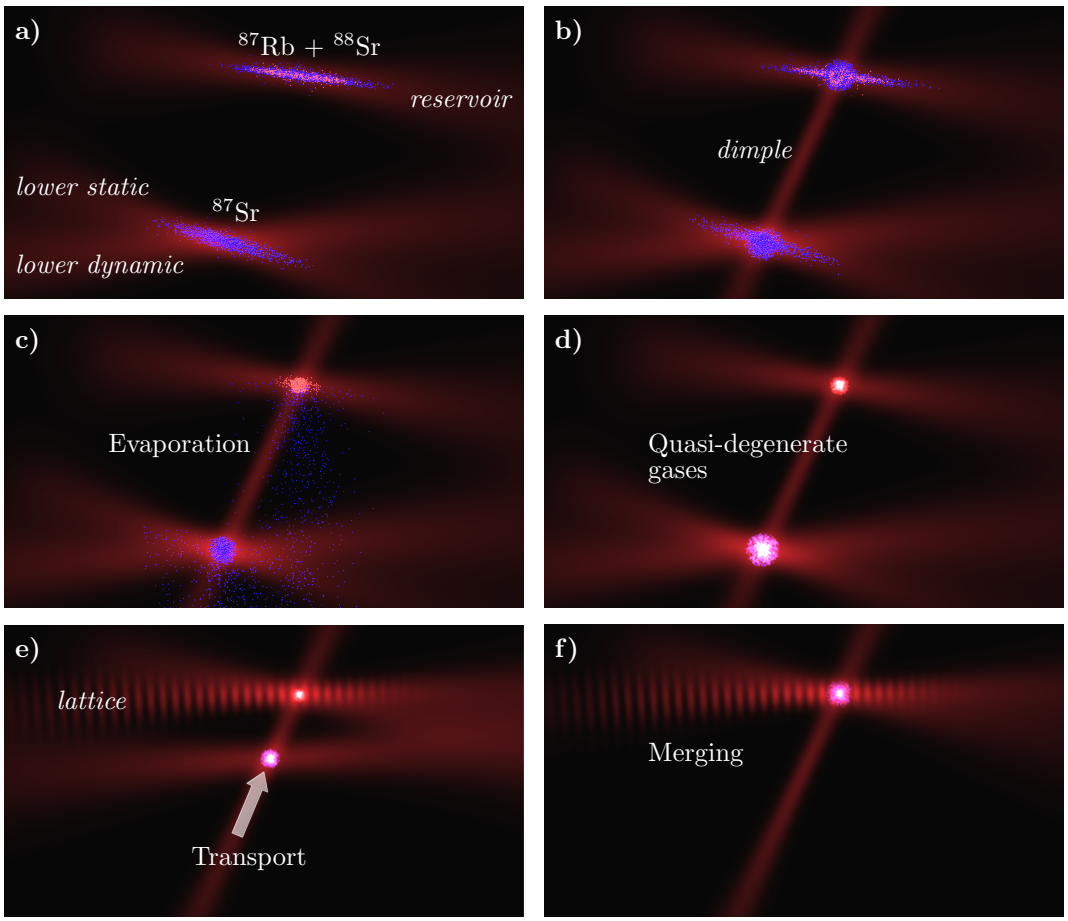


Figure 2.4: Illustration of the experimental sequence during in-trap cooling and merging of the atomic clouds. The names of the dipole traps are in *italic*. Once ^{87}Rb and ^{88}Sr have been loaded in the reservoir trap and ^{87}Sr in the lower traps (a), the connecting dimple is switched on (b). The intensity of the horizontal traps is decreased during the evaporation stage (c) and we are left with quasi-degenerate gases (d). A piezo-mirror moves the lower dynamic trap and ^{87}Sr moves along the dimple (e). At the same time the optical lattice is ramped up on the Rb cloud. Finally the atomic clouds merge in the crossing point of reservoir, lattice and dimple traps. Credits to Digvijay for the illustrations (adapted).

Chapter 3

1D optical lattice

The ability to engineer potentials using light has become an invaluable tool in the field of ultracold quantum gases. In the RbSr experiment, we employ four dipole traps in combination with a one-dimensional optical lattice. The lattice plays a crucial role in two respects: it stabilizes the resonantly interacting ^{87}Rb–^{87}Sr mixture and enables us to attempt molecule association via a confinement-induced resonance. I will discuss these topics in Section 3.1. Section 3.2 presents the theoretical background of off-resonant optical trapping. Section 3.3 describes two methods we used to characterize the lattice. Finally, Section 3.4 describes the issues we encountered while testing the 1D optical lattice and the steps we took to debug and fix them.

3.1 Motivation

Imposing strong confinement along a single direction can modify the properties of the ensemble. In this section, I discuss two effects that we exploit in our experiment. The first is the stabilization of a resonantly interacting mixture. The second effect enables the mixture to access the first bound molecular state via a so-called confinement-induced resonance.

3.1.1 Confinement induced stabilization of the mixture

Resonantly interacting ultracold gases are powerful platforms for studying strongly correlated few- and many-body physics, but their practical utility is severely limited by rapid atom loss through three-body recombination. In three-body collisions, a dimer is formed during the collision, and the third atom gains kinetic energy equivalent to the binding energy of the dimer. Both the dimer and the atom are lost as the first one is typically no longer trapped and the atom has a large kinetic energy. In Bose-Bose and Bose-Fermi mixtures — unlike Fermi gases, which benefit from Pauli suppression, three-body losses are particularly problematic, especially in alkali-alkaline-earth systems where Feshbach resonances are too narrow.

In this section I briefly show experimentally that confining a ^{87}Rb -^{87}Sr mixture to a quasi-2D regime via a 1D optical lattice dramatically extends the mixture's lifetime. Whereas the 3D system suffers rapid heating and atom loss, the quasi-2D system achieves lifetimes of several hundred milliseconds out significant heating (fig.3.1), while maintaining strong two-body interactions [37]. This modification

reduces the wave-function overlap between the initial free-atom state and the final atom-dimer state, introducing an energy-dependent suppression term and yielding an estimated reduction of $\sim 10^5$ in the three-body recombination rate [38]. Crucially, unlike in 3D where the rate remains finite at low energies, the 2D rate vanishes in the low-energy limit.

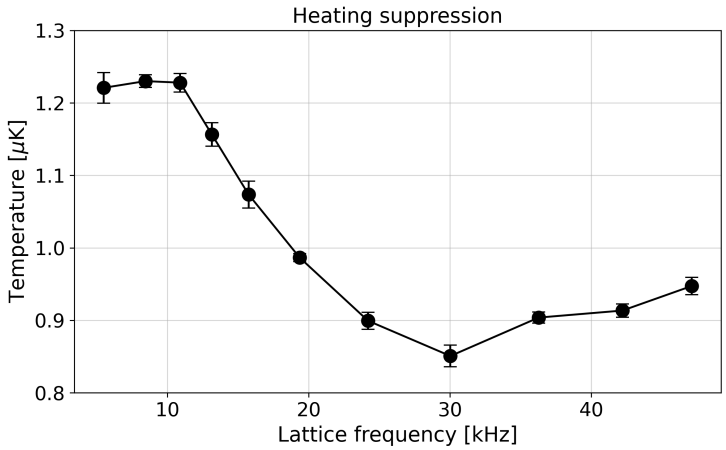


Figure 3.1: 3D to 2D regime crossover. To distinguish between the 3D and 2D regimes, we measure ^{87}Sr temperature 220 ms after merging the two species. We observe a relatively sharp crossover between the two regimes at a lattice frequency of about 20 kHz. The reported lattice frequency corresponds to Sr frequency.

Beyond the specific ^{87}Rb–^{87}Sr system, this confinement-induced stabilization strategy is broadly applicable to other mixtures with resonant scattering lengths, including systems without accessible magnetic Feshbach resonances. The approach also opens perspectives for mixed-dimensional engineering exploiting the different polarizabilities of the two species, and for adiabatic molecule creation via confinement induced resonances as an alternative to magnetoassociation.

3.1.2 Confinement induced resonance

As previously discussed, interspecies magnetic Feshbach resonances, standard tool for molecule formation in bi-alkali mixtures, are practically not usable in our mixture. By choosing the isotope combination with the highest s-wave scattering we can hope to be able to use a so-called *confinement induced resonance* (CIR).

CIRs arise from the anharmonicity of the trapping potential, which couples the relative and center-of-mass motion of two confined atoms[36]. When the energy of an unbound atom pair becomes resonant with that of a center-of-mass-excited molecular bound state, coherent coupling between the two states enables the association of atom pairs into weakly bound molecules. These Feshbach-like molecules constitute an excellent starting point for subsequent optical transfer schemes, as their significantly increase the Franck-Condon overlap with electronically excited molecular states.

Following from eq.2.2, the first bound state in the ^{87}Rb–^{87}Sr molecular potential should be just $h \times 20.5$ kHz below the continuum. This energy is easily within reach by optical confinement. In the case RbSr it has been shown that CIRs can arise

in a quasi-1D potential even if they experience different trap frequencies due to different polarizabilities at 1064 nm [11]. For this reason, one of the next steps of the experiment would be to add a second lattice to produce a confinement in two directions.

3.2 Theory of optical lattices

Light can interact with atoms through both dissipative and conservative forces. Dissipative forces are exploited, for example, in optical molasses [39], where radiative pressure arises from the repeated absorption and emission of photons by the atoms. Such forces typically rely on near-resonant light.

In contrast, conservative forces can be generated using off-resonant light[40]. These forces originate from the dipole moment induced in an atom or molecule by an external electric field. Depending on the detuning, the resulting force can be either attractive or repulsive. Potentials created in this way are commonly referred to as optical dipole traps (ODTs). The derivation below follows mostly [40].

3.2.1 Optical dipole traps

When an atom is placed in an oscillating electric field $\mathbf{E}$ oscillating at frequency ω such as a laser field, the electronic cloud deforms and exhibits an induced dipole moment $\mathbf{d}$. The dipole moment oscillates at the field frequency with an amplitude given by

$$|\mathbf{d}| = \alpha(\omega)|\mathbf{E}|\,, \tag{3.1}$$

where the complex proportionality factor $\alpha(\omega)$ is the atom polarizability and depends on ω. The real component of alpha determines the dispersive response while the imaginary component determines the dissipation and absorption.

The time averaged interaction energy of the dipole with the electric field is

$$V_{dip} = -\frac{1}{2}\langle \mathbf{dE}\rangle = -\frac{1}{2\epsilon_0 c}\mathrm{Re}(\alpha)I\,, \tag{3.2}$$

where

$$I = \frac{1}{2}\epsilon_0 c|E|^2\,. \tag{3.3}$$

For a beam intensity profile $I(r)$, we obtain a position dependent potential $V_{dip}(r)$. The dipole force results form the gradient of the potential:

$$\mathbf{F}(r) = -\nabla V_{dip}(r) = \frac{1}{2\epsilon_0 c}\mathrm{Re}(\alpha)\nabla I(r)\,. \tag{3.4}$$

Another quantity of interest is the power absorbed by the atom from the light field,

$$P_{\mathrm{abs}} = \langle \dot{\mathbf{d}}\mathbf{E}\rangle = \frac{\omega}{\epsilon_0 c}\mathrm{Im}(\alpha)I\,. \tag{3.5}$$

For an ideal optical dipole trap, the interaction should be purely conservative, minimizing the amount of energy absorbed by the atoms in order to avoid heating. The corresponding photon scattering rate is

$$\Gamma_{\mathrm{sc}} = \frac{P_{\mathrm{abs}}}{\hbar\omega} = \frac{1}{\hbar\epsilon_0 c}\mathrm{Im}(\alpha)I\,. \tag{3.6}$$

To relate the polarizability to the properties of the atom and the light field, the atom can, to first approximation, be modeled as a classical damped harmonic oscillator following Lorentz theory. This leads to the expression

$$\alpha(\omega) = 6\pi\epsilon_0 c^3 \frac{\Gamma/\omega_0^2}{\omega_0^2 - \omega^2 - i\Gamma(\omega^3/\omega_0^2)}\,, \tag{3.7}$$

where Γ is the spontaneous decay rate of the excited state and ω_0 is the resonant frequency. If we now express the potential and the off-resonance scattering rate in the rotating wave approximation using Eq.3.7 we get:

$$V_{dip} = \frac{3\pi c^2}{2\omega_0^3}\left(\frac{\Gamma}{\Delta}\right) I(r)\,, \tag{3.8}$$

$$\Gamma_{sc} = \frac{3\pi c^2}{2\hbar\omega_0^3}\left(\frac{\Gamma}{\Delta}\right)^2 I(r)\,. \tag{3.9}$$

An important feature is the different dependence on the detuning Δ. The dipole potential scales as $1/\Delta$, whereas the scattering rate scales as $1/\Delta^2$. As a result, sufficiently large detunings allow significant trapping forces while strongly suppressing photon scattering.

The sign of the detuning also determines the nature of the force. For red-detuned light ($\Delta < 0$), the potential is negative and the force is attractive, causing atoms to accumulate in regions of high intensity. For blue-detuned light ($\Delta > 0$), the potential is positive and the force becomes repulsive. In practice, red-detuned optical dipole traps are more commonly used because they only require a tightly focused high-power laser beam. Blue-detuned configurations are also possible, for example in so-called box potentials, where atoms are confined inside a dark region surrounded by repulsive light sheets.

From an experimental perspective, the dipole potential is often written in terms of the measured polarizability:

$$V_{dip} = \frac{1}{2}\alpha Z_0 I(r)\,, \tag{3.10}$$

where $Z_0 = \sqrt{\mu_0/\epsilon_0} = 376.73\,\Omega$ is the vacuum impedance.

To achieve stronger confinements, beams are typically focused down to few tens or hundreds of μm. Intensities of W/cm^2 can be easily obtained. A consequence of such approach is that the waist of the beam in not constant along the propagation axis, which means that the trapping force depends on the distance from the focus. The spatial intensity distribution is then described by

$$I(r,z) = \frac{2P}{\pi\omega^2(z)} \exp\left(-\frac{2r^2}{\omega^2(z)}\right)\,, \tag{3.11}$$

where P is the source power and $\omega(z)$ is the $1/e^2$ radius defined as

$$\omega(z) = \omega_0\sqrt{1 + \left(\frac{z}{z_R}\right)^2}\,, \tag{3.12}$$

with z_R being the so called *Rayleigh range*, defined as $z_R = \pi\omega_0^2/\lambda$. The Rayleigh range provides a characteristic length scale for how rapidly the potential varies along

the propagation axis. A tighter focus corresponds to a smaller z_R, leading to more rapid changes in the potential. This is experimentally important, as it determines the order of magnitude of the precision required for positioning the focal point along the axial direction.

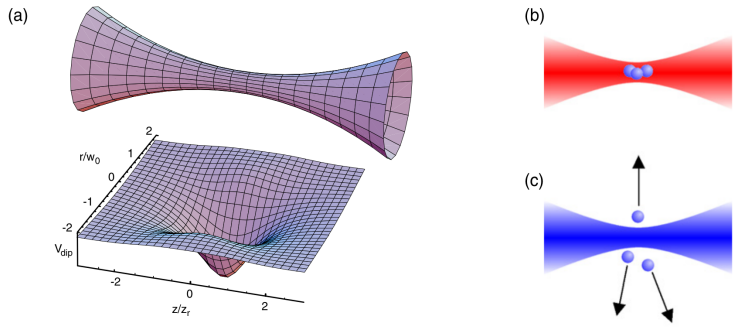


Figure 3.2: a) Schematic illustration of a focused Gaussian beam shown together with a cross section of the corresponding trapping potential for a red-detuned trap. The trap provides strong radial and weak axial confinement (aspect ratio of the potential profile not drawn to scale). b) In a red-detuned dipole trap, atoms are localized at the intensity maximum. c) In a blue-detuned dipole trap, atoms are repelled from regions of high intensity. From [41].

If the thermal energy k_BT of the atomic ensemble is much smaller than the potential depth V_0, the extension of the atomic sample is radially small compared to the beam waist and axially small compared to the Rayleigh range. In this case, the optical potential can be well approximated by a simple cylindrically symmetric harmonic oscillator

$$V_{dip}(r,z) \approx V_0 \left[1 - 2\left(\frac{r}{\omega_0}\right)^2 - \left(\frac{z}{z_R}\right)^2\right]. \tag{3.13}$$

with $V_0 = V_{dip}(r=0)$ from eq (3.8), i.e. in the center of the focus. The oscillation frequencies of a trapped atom are given by $\omega_r = \sqrt{4V_0/m\omega_0^2}$ in the radial direction, and $\omega_z = \sqrt{2V_0/mz_R^2}$ in the axial direction.

3.2.2 Optical lattice

One of the simplest and most used potentials is the so called optical lattice. The simplest version of such lattice potentials are obtained by retro-reflecting a single red-detuned gaussian beam trap. For this reason they are referred to as 1D optical lattices.

Consider a focused gaussian beam. Retroreflecting the beam makes it interfere with itself, creating an interference pattern or standing wave. The resulting potential is

$$V_{latt}(r,z) = 4V_{dip}(r,z)\cos^2(kz) \approx 4V_0\cos^2(kz)\left[1 - 2\left(\frac{r}{\omega_0}\right)^2 - \left(\frac{z}{z_R}\right)^2\right], \tag{3.14}$$

which is the same expression as (3.13) with a periodic modulation. Because of the constructive and destructive interference, the potential spans between $4V_0$ and 0

within half a wavelength along the axial direction. This creates a strong confinement in this direction, yielding a trapping frequency of $\omega_z = \sqrt{8V_0/m\lambda^2}$ at the focus.

At low temperatures and high laser powers, the zero-point energy $\frac{1}{2}\hbar\omega_z$ becomes comparable with the thermal energy $\frac{1}{2}k_BT$ of the atoms. in such conditions, the dimensionality of the system is closer to 2D. In addition, if the wavepacket spread becomes smaller than the scattering length, the scattering properties of the sample can change dramatically as we shall see in the next section.

Finally, one could think of overlapping more optical lattices in order to create more complex potentials (for example see [41]). Adding a second lattice perpendicular to the first one, gives rise to a tube or "cigar" shaped potentials close to a set of 1D systems. Adding a third perpendicular beam creates a cubic lattice. Such potentials are widely used in quantum simulation and quantum computing experiments [2].

3.3 Lattice characterization methods

Estimating the lattice depth knowing the laser power and the size of the laser beam is pretty straightforward. Nevertheless it is good practice to always crosscheck the result with some measurements with the atoms since, as we will see, there are still many important details that can go wrong. In this section I will describe two methods that we exploited to estimate the lattice frequencies in our experiment. The first one is called *parametric heating* and measures the resonant oscillation frequency of the atoms in the trap. The second one is Kapitza-Dirac BEC diffraction in Bragg regime, where the periodic potential imposes a ladder structure in momentum space.

3.3.1 Parametric heating

If the thermal energy of the atomic cloud is much smaller than the trapping potential, *i.e.* $k_BT \ll V_0$, the cloud is confined near a minimum of the optical lattice well and the atomic motion can be approximated as that of a harmonic oscillator with frequency ω_{lat} [42]. If the lattice depth is modulated in time, the curvature of the potential — and therefore the trap frequency — becomes time-dependent. Writing the modulation as

$$V_0(t) = V_0\left[1 + \epsilon\cos(\omega_{\text{mod}}t)\right], \qquad \epsilon \ll 1, \tag{3.15}$$

the equation of motion for an atom of mass m reads

$$m\ddot{x} + m\omega_{\text{lat}}^2\left[1 + \epsilon\cos(\omega_{\text{mod}}t)\right]x = 0. \tag{3.16}$$

This is the equation of a parametrically driven harmonic oscillator, belonging to the class of Mathieu equations. Similarly to a classic driven harmonic oscillator, where the driving force appears as an additive term, the solutions of the Mathieu equation exhibit instability regions where the amplitude grows exponentially in time. The dominant instability occurs when the modulation frequency satisfies

$$\omega_{\text{mod}} \approx 2\omega_{\text{lat}}, \tag{3.17}$$

which can be understood intuitively: the system absorbs energy most efficiently when the trap is modulated at twice its natural oscillation frequency. This exponential

increase corresponds to a continuous transfer of energy from the modulation into the atomic motion.

Using the harmonic approximation, the lattice frequency is related to the lattice depth V_0 by

$$V_0 = \frac{m\omega_{\text{lat}}^2}{2k_{\text{lat}}^2}, \tag{3.18}$$

so that the measured resonance position provides a direct calibration of V_0.

In practice, the lattice intensity (and hence V_0) is modulated for a fixed hold time over a range of frequencies ω_{mod}. After modulation, the lattice is switched off and the atomic cloud is released; The experimental observables are heating and atoms loss. This approach is robust because it relies only on the dynamical response of the system and does not require precise knowledge of the experimental parameters, relying only on harmonic approximation.

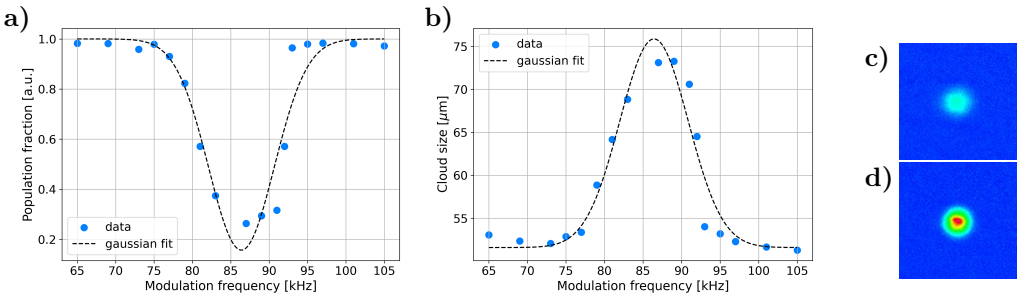


Figure 3.3: Example of parametric heating measurement. After loading the atomic cloud into the optical lattice, we modulate the intensity of the light. When the modulation frequency coincides with twice the lattice frequency, the system absorbs energy and heats up. Consequently, we observe (a) a loss of atoms from the trap and (b) an expansion of the cloud. Panels (c) and (d) present images of the cloud driven at resonant and off-resonant frequencies respectively.

We make use of parametric heating also for a different purpose. Given the different polarizabilities of Rb and Sr at 1064 nm, the two atomic species experience different trapping forces and therefore different oscillating frequency for a given lattice. We exploit this fact to check that the Rb cloud and the Sr cloud are overlapping by measuring a strong parametric heating feature in Sr at Rb frequency. This is only due to good inter-species thermalization, since if we do not load Rb in the trap the feature in Sr disappears.

3.3.2 Kapitza-Dirac BEC diffraction in Bragg regime

A second method for calibrating the lattice depth is based on the coherent diffraction of a BEC by a short pulse of the standing-wave light field. A BEC in free space is well described as a plane wave $|\Phi_q\rangle$ of quasi-momentum q [43]. This approximation is justified because the condensate typically extends across many lattice sites, so the wavefunction is nearly uniform on the scale of the lattice period.

When the lattice is switched on abruptly, the initial BEC state $|\Phi_q(t = 0)\rangle$ is projected onto the instantaneous n-th Bloch eigenstates $|n_B, q\rangle$ of the lattice

Hamiltonian:

$$|\Phi_q(t=0)\rangle = \sum_{n_B=0}^{\infty} |n_B, q\rangle\langle n_B, q|\Phi_q\rangle \,. \tag{3.19}$$

Using the plane-wave expansion of Bloch states (Eq. 4.11), this becomes

$$|\Phi_q(t=0)\rangle = \sum_{n_B=0}^{\infty} c^*_{l_{\mathrm{BEC}},n_B,q}\, |n_B, q\rangle \,, \tag{3.20}$$

where $l_{\mathrm{BEC}} = (q-p)/(2\hbar k) = 0$ for a BEC at rest. The coefficients $c^*_{0,n_B,q}$ are the plane-wave components of each Bloch state projected onto the BEC at rest.

After the lattice is switched on, the state evolves under the lattice Hamiltonian $\hat{H}_{\mathrm{latt}}$. Applying the time-evolution operator $\exp(-i\hat{H}_{\mathrm{latt}}\, t/\hbar)$ to Eq.(3.20), the state at time t is

$$|\Phi_q(t)\rangle = \sum_{n_B=0}^{\infty} c^*_{0,n_B,q}\, \exp(-iE_{n_B,q}\, t/\hbar)\; |n_B, q\rangle \,. \tag{3.21}$$

For a BEC initially at rest ($q = 0$) as in our case, only even bands are populated during the subsequent evolution. This follows from the symmetry of the Bloch states: the BEC wavefunction is symmetric across a lattice site, and only even-band Bloch states at $q = 0$ have this symmetry.

When the lattice pulse is switched off abruptly after a pulse time t_{lp}, the state $|\Phi_q(t_{\mathrm{lp}})\rangle$ is projected back onto the free-space plane-wave basis $|\phi_{q+2l\hbar k}\rangle$, corresponding to diffraction orders $l = 0, \pm1, \pm2, \ldots$ This projection constitutes the measurement: atoms in order l are detected as a separate peak in time-of-flight imaging. The population amplitude of diffraction order l is

$$b_{l,q}(t_{\mathrm{lp}}) = \langle \Phi_{q+2l\hbar k}|\Phi_q(t_{\mathrm{lp}})\rangle = \sum_{n_B=0}^{\infty} c^*_{0,n_B,q}\, c_{l,n_B,q}\, \exp(-iE_{n_B,q}\, t_{\mathrm{lp}}/\hbar) \,. \tag{3.22}$$

For $V_{\mathrm{latt}} \lesssim 10\, E_{\mathrm{rec}}$, contributions from bands $n_B \geq 4$ and from momentum states $|l| \geq 2$ are negligible. The sum in (3.22) therefore truncates to two terms, $n_B = 0$ and $n_B = 2$, and the amplitude of diffraction order l becomes

$$b_{l,q=0}(t_{\mathrm{lp}}) \approx c^*_{0,0,0}\, c_{l,0,0}\, e^{-iE_{0,0}\, t_{\mathrm{lp}}/\hbar} + c^*_{0,2,0}\, c_{l,2,0}\, e^{-iE_{2,0}\, t_{\mathrm{lp}}/\hbar} \,. \tag{3.23}$$

The population of order l is $P_l = |b_{l,q=0}|^2$. Defining the global phase factor $e^{-iE_{0,0}t_{\mathrm{lp}}/\hbar}$ (which cancels in the modulus squared) and the frequency

$$\omega_{\mathrm{lp}} = \frac{E_{2,0} - E_{0,0}}{\hbar} \,, \tag{3.24}$$

equation (3.23) can be written as

$$b_{l,q=0}(t_{\mathrm{lp}}) \propto c^*_{0,0,0}\, c_{l,0,0} + c^*_{0,2,0}\, c_{l,2,0}\, e^{-i\omega_{\mathrm{lp}}\, t_{\mathrm{lp}}} \,. \tag{3.25}$$

Taking the squared modulus and using $A = c^*_{0,0,0}\, c_{l,0,0}$, $B = c^*_{0,2,0}\, c_{l,2,0}$ for brevity:

$$P_l(t_{\mathrm{lp}}) = |A|^2 + |B|^2 + 2\,\mathrm{Re}(AB^*)\cos(\omega_{\mathrm{lp}}\, t_{\mathrm{lp}}) + 2\,\mathrm{Im}(AB^*)\sin(\omega_{\mathrm{lp}}\, t_{\mathrm{lp}}) \,. \tag{3.26}$$

The population of each diffraction order therefore oscillates during the pulse at the single frequency ω_{lp}. This is analogous to coherently driving a two-level system, in which the role of the two states is played by the $n_B = 0$ and $n_B = 2$ Bloch bands. When the lattice is switched off and the state is projected onto plane waves, this accumulated phase appears as oscillations in the diffraction order populations.

In the experiment we measure the population of one of the diffracted orders for different pulse times (fig.3.4) and plot the population fraction as $P_1 = N_1/N_{tot}$. The oscillation frequency is extracted by fitting a sinusoidal function. The lattice frequency is estimated by computing the eigenvalues of the Hamiltonian in an optical lattice of variable depth. The lattice depth is then fixed by imposing that $E_{2,0} - E_{0,0}$ corresponds to the measured value.

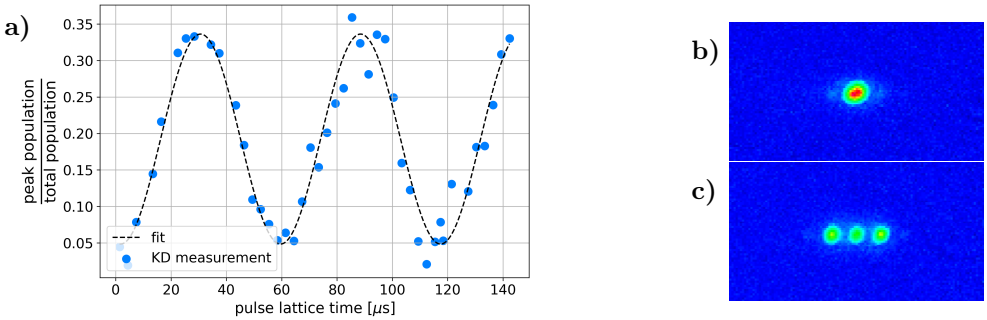


Figure 3.4: Measurement of coherent oscillations of the diffraction peaks populations. Panel (a) shows the oscillations of one of the $\pm 2\hbar k$ peaks. Panels (b) and (c) show two absorption images of the population distributions respectively when all the atoms are in the 0-order and when population is equally distributed between the three orders.

3.4 Debugging sequence

As mentioned before, we encountered some problems while characterizing the 1D optical lattice. In this section I will describe the starting condition and our efforts to find and fix the problem.

The lattice frequency obtained with the parametric heating (PH) method (Section 3.3.1) was roughly 40% of the theoretically expected value. Suspecting an error in the measurement procedure, we decided to carry out an independent measurement using a completely different technique: Bragg scattering (BS) of a Rb BEC (Section 3.3.2). This second method produced results that agreed with the previous PH measurements. At that point, we began to suspect an issue with the experimental implementation itself and carefully rechecked all experimental parameters, including beam shape, waist size, power, polarization and alignment, but everything appeared correct. After many further debugging attempts, we converged on the hypothesis that the problem could be related to the coherence of the light. Indeed, after some dedicated effort, we managed to directly observe the interference pattern and found that its contrast was very poor. The amplifier was found to have a broad frequency background in it's spectrum (measurement in section 3.4.2) and hence there was less power in the frequency component of interest for the optical lattice. The only viable solution was to replace the amplifier. The new amplifier generated

an interference pattern with very high contrast. Once it was integrated into the experiment, we were able to measure lattice frequencies that were about 80% of the expected values. We attribute this discrepancy to factors such as an imperfect estimation of the beam waist, a slight offset from the focus, and to the non perfect polarization. In this section, I will describe each of these steps.

Because we had difficulty finding a fully worked-out lattice frequency example with all the numerical values needed to verify that our code was correct, I will present every detail of our own setup. The optical lattice is generated by retro-reflecting a few watts from a 1064 nm laser amplifier (NKT Boostik, 15 W). This amplifier is seeded with approximately 20 mW of light provided either by a Mephisto MOPA or by an Azur Light fiber laser (ALS).The lattice beam has a waist size in the focus $\omega_0 \approx 130\,\mu$m and a Rayleigh range $z_R \approx 5\,$cm. The maximum power out of the last fiber is 5.2 W but we should consider the reflections of the glass cell where the experiment takes place since it in not AR coated for IR light. Every time the beam passes through the cell about 9% of the light gets reflected out. This leaves us with an effective power of $P_{\max} \approx 5.2\,\mathrm{W} \cdot (0,91)^3 = 3.92\,\mathrm{W}$ after crossing three times the glass walls. The maximum intensity is $I_{\max} = 2P_{\max}/\pi\omega_0^2 \approx 1.5 \times 10^4\,\mathrm{W/cm^2}$. Given this numbers, one can easily estimate the maximum lattice dept as $4V_{dip} \approx 1.12 \times 10^{-27}\,\mathrm{J}$ from eq.(3.8) by considering the closest and strongest transition(s), or $4V_{dip} \approx 1.26 \times 10^{-27}\,\mathrm{J}$ from eq.(3.10) by using measured values of α [28]. Lastly, the maximum lattice frequency is calculated to be 117 kHz or 124 kHz, depending on which value of the lattice depth one uses.

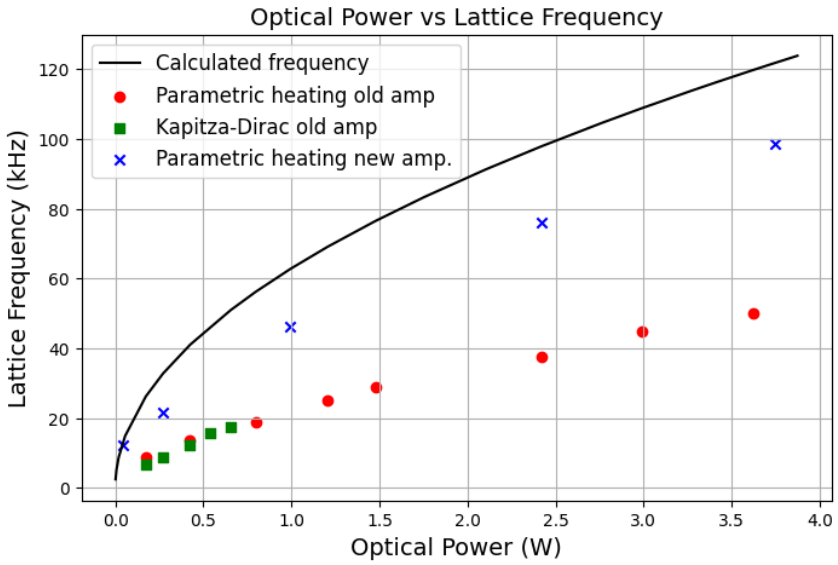


Figure 3.5: Optical power versus calculated and measured frequencies. The solid black line represents the frequencies calculated using eq.3.14, the dots correspond to frequencies measured via the parametric heating method, and the stars correspond to those measured with the Kapitza–Dirac method. The data obtained with the old amplifier are internally consistent but fall at less than half of the predicted value. The measurements taken with the new amplifier are consistent, and lie much closer to the expected values, even if there is still a significative discrepancy.

We tune the optical power via the control system by adjusting the attenuation of the RF signal driving the AOM. Figure 3.6 presents its characterization.

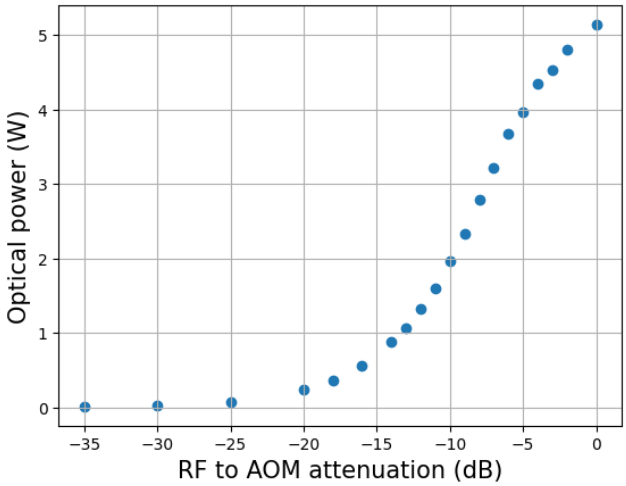


Figure 3.6: characterization of the optical power in the lattice beam with respect to the attenuation of the RF power driving the AOM. The Rf signal can be generated at different powers from a Direct Digital Synthesis (DDS) module. The signal is then fed into an amplifier that increases the power by $\approx 30\,\mathrm{dB}$ and finally in the AOM that determines the amount of light that falls in the diffracted orders.

The frequencies that we measured both with PH and BS were about 40% of what we calculated (fig.3.5). After spending some time double checking both the calculations and the experimental parameters we started suspecting that the problem might have been the laser light itself. We started debugging by damping the light before it got reflected back. We were left with a simple single beam dipole trap. We could perform a so called Center of Mass (COM) oscillations measurement. The depth of the trap is calculated by measuring the oscillation frequency of the cloud around the minimum of the potential.

After loading a very cold Rb cloud (few μK) into the reservoir trap, we ramp up our single lattice beam. We put the atomic cloud in motion by suddenly switching off the reservoir trap. After waiting a variable amount of time we switch off the single lattice beam and record the position of the cloud. We could clearly measure the oscillation frequency of the COM in the dipole trap (fig.3.7). The measured frequencies are of the order of hundred of Hz and matched with the calculated ones.

The next step consisted in allowing the retroreflection but through a $\lambda/4$ waveplate. The retro reflected component of the beam had a linear polarization orthogonal to the one of the incoming beam. In practice this means doubling the power of the dipole trap without building any interference pattern. We again measured COM oscillations and the matched with the expected value. At this point we could say with some confidence that the power, the waist and the alignment of the lattice beam were not causing the problem. We also checked that the polarization was nice and linear in every section of the beam path with a polarizing beam splitter.

By simply removing the waveplate we should have seen a perfect contrast lattice, which again failed to show up both with PH and BS measurements. At this point we started suspecting the coherence of the light.

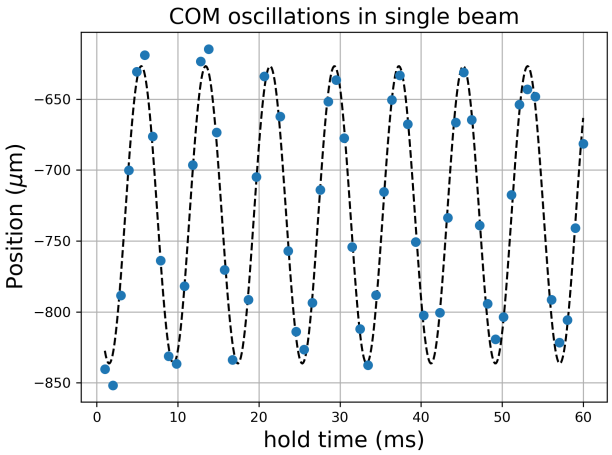


Figure 3.7: Example of a center of mass oscillations measurement. The blue dots are the measured positions (after 7 ms of flight) for different hold times in the single dipole beam. The dashed line is the fitted oscillation from which we calculate the frequency.

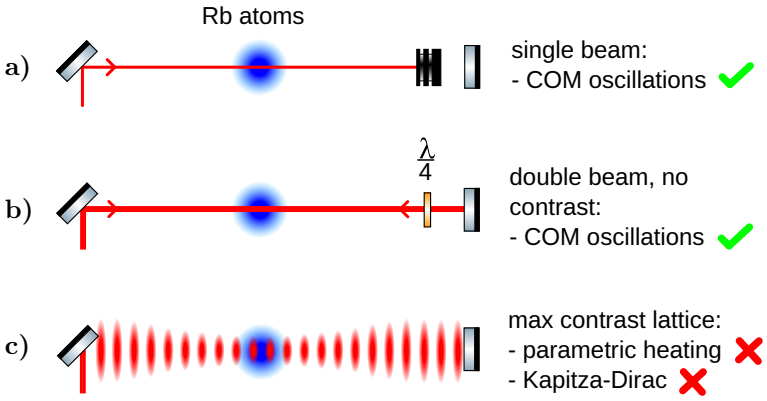


Figure 3.8: Center-of-mass oscillation measurement sequence. In the first experiment (a), we damped the beam before it was retro-reflected, leaving only a single-beam dipole trap. The measured oscillation frequency agreed with the calculated value. In the second experiment, we allowed the retro-reflection but inserted a quarter-wave plate into the optical path. This made the polarizations of the incident and reflected beams orthogonal, suppressing interference formation. As a result, we obtained a dipole trap with twice the intensity, and again the measured frequency matched the expected one. By simply removing the wave plate, an interference pattern should form (c). However, both parametric heating and Kapitza–Dirac BEC diffraction measurements produced frequencies lower than expected.

3.4.1 Lateral displacement prism and fringes method

The first attempt to investigate the spectral quality of the light was done with a Fabry-Perot cavity. We expected the light not to be single mode and show some other peaks other than the main one. Unfortunately, we saw a single peak (fig.3.9) without any unexpected feature. We could then say that the laser was single frequency, unless, there was a very broad background noise that would hardly enter the cavity due to its single mode nature.

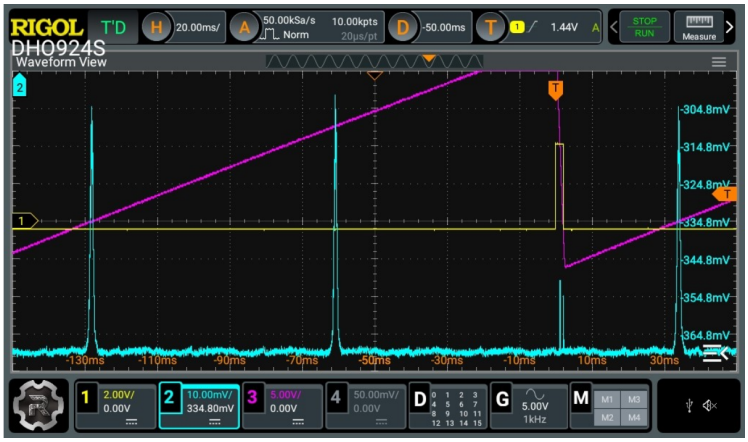


Figure 3.9: Spectrum of the light coming out of the amplifier recorded with the Fabry-Perot cavity (blue signal). The absence of secondary peaks tells us that it is mostly single mode. At the same time the transmission signal through the cavity is not sensitive to broad band background noise because it only couples to the cavity weakly and in a length-independent way.

The turning point happened to be the discovery of a Lateral Displacement Prism (LDP). An LDP functions as a 50:50 beam splitter that generates two parallel beams with equal power. It is commonly employed, together with a long focal length lens, to produce a so-called shallow-angle lattice. At the focal plane, the two beams overlap and form an interference pattern. This setup is analogous to a double-slit experiment, where the spacing Δl between adjacent interference maxima in the focal plane is determined by the optical path length difference and can be calculated using the relation:

$$\Delta l = f\lambda/nd \approx 14\,\mu\text{m}\,, \tag{3.27}$$

where $f = 200$mm is the focal length, $n = 1.5$ the refractive index of the glass and $d = 10\,$mm is the separation between the two beams. The pixel size of the camera (Thorlabs CS165MU) is $3.45\,\mu$m, which is just enough to resolve the diffraction pattern with slightly more than 4 pixels per period. As we will see, it still shows a good contrast pattern also for shorter wavelengths (fig.3.11). In order to make the measurements faster and more reproducible, I built a small portable setup (fig.3.10). It is composed by a collimator, the LDP and a 200 mm lens focusing on the camera. By including a $\lambda/2$ waveplate and a PBS one can easily control the intensity of the beam on the camera by damping part of the light. I could easily carry this compact instrument around and measure the interference pattern of any laser by simply plugging in a fiber with few mW. I measured patterns from lasers with

different linewidths and different wavelengths to be sure that I was not limited by these parameters.

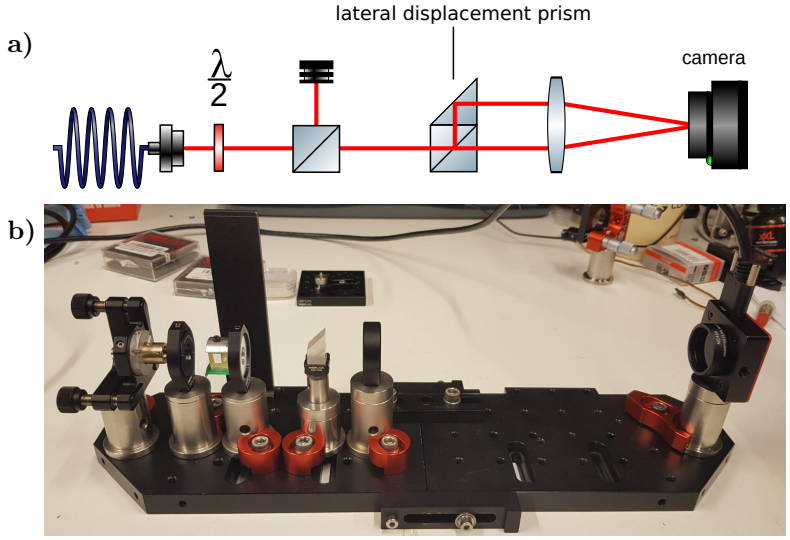


Figure 3.10: (a) Schematics of the instrument used to record the fringes patterns. The combination of half waveplate and PBS makes it possible to dump part of the light in order to not saturate the camera. The interference pattern is obtained by splitting the light into parallel beams with the lateral displacement prism and recombine them with a lens. The pattern is recorded with a CMOS camera placed on the focal plane. (b) Picture of the instrument. Its small size allowed to easily carry it around and test many different laser sources.

To quantify the contrast we calculated the Michelson visibility defined as

$$v = \frac{I_{\max} - I_{\min}}{I_{\max} + I_{\min}}, \tag{3.28}$$

with $I_{\max}$ being the maximum value of the interference pattern and $I_{\min}$ the adjacent minimum of the pattern. The old amplifier yielded a visibility of 21%. Luckily enough, we had a brand new amplifier of the very same model. We injected it with the same seeds and the resulting visibility was 87% (fig.3.11b). Also the 1064 nm sources we use for seeding the amplifiers yielded visibilities close to 87% (fig.3.11c/d). I recorded the interference pattern using 689 nm light (fig.3.11e) to check whether the camera's resolution was the limiting factor. The visibility at 689 nm is about 90%, indicating that we are barely constrained by the camera's resolution.

This method demonstrated that the mismatch between the calculated and measured lattice frequencies originates from poor light coherence. The issue was traced to the amplifier, as the seed light itself was functioning correctly. This outcome was surprising, given that the amplifier had been purchased only a year earlier. Its specified linewidth is below 3 kHz, implying a coherence length on the order of kilometers. However, our measurements with the LDP indicated a coherence length of less than 1.5 cm for a significant fraction of the light.

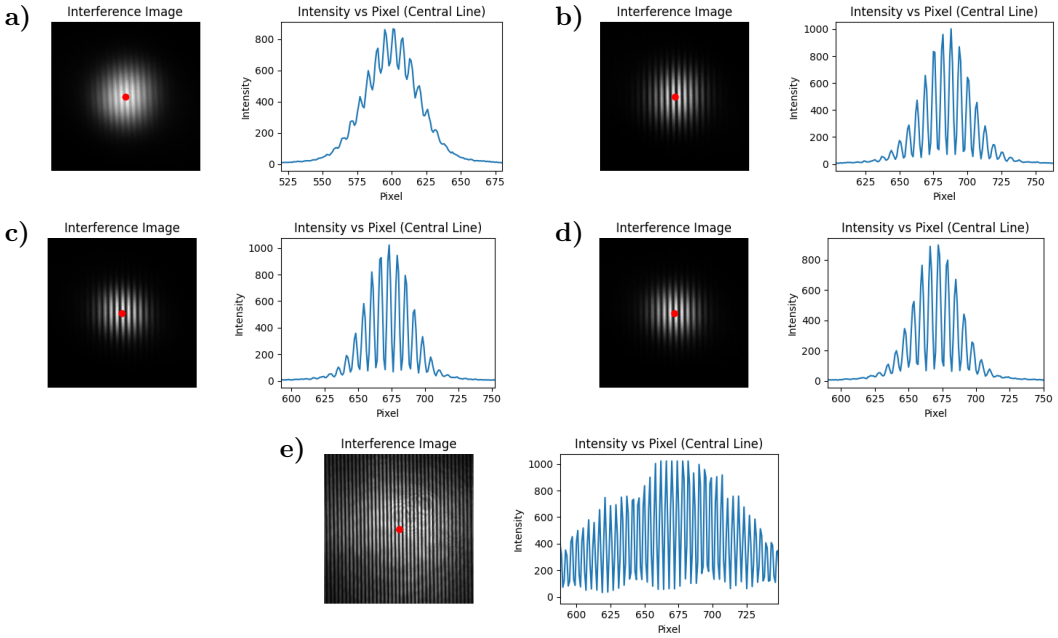


Figure 3.11: Recorded interference patterns for different laser sources. Panels (a) and (b) show the patterns from the old and the new amplifier respectively. The measured visibility of the old amplifier is around 20% which matches with the measured lattice depths. On the other hand the new amplifier shows 87% visibility, similar to the visibility of Mephisto (c) and ALS (d) seeds. This allows us to say that while the new amplifier inherits the characteristics of the seeds, the old one does not. Panel (e) shows the interference pattern of a 689 nm light source. The measured visibility of 90% tells us that we are barely limited by the resolution of the camera at 1064 nm.

3.4.2 Phase noise characterization

The fringes test revealed that the 1.5 cm of optical path difference introduced by the LDP was enough to ruin almost completely the coherence of the light. A rough estimate tells us that the light is noisy at the $c/nd \approx 20\,\text{GHz}$ level. At the same time, the Fabry-Perot cavity and the fringes pattern told us that there was still a coherent component in the light.

To conclude this section, we wanted to characterize the phase noise of the amplifier. I built a Michelson interferometer with a double pass AOM in one of the two arms and recorded the beat signal on a photo diode (PD) (fig.3.12).

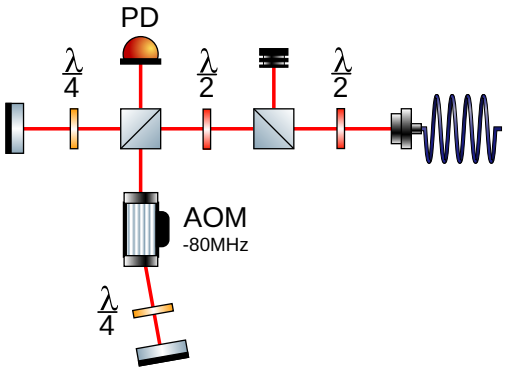


Figure 3.12: Schematics of the setup used to record the beat signal. It consists in a Michelson interferometer with a double pass AOM in one of the two arms, which introduces a frequency shift of $2 \times 80\,\text{MHz}$. The beatnote signal is recorded with a commercial photodiode on a spectrum analyzer. Since we want to measure high frequency noise ($\gtrsim 10\,\text{MHz}$) a path length difference of $\approx 20\,\text{cm}$ is sufficient.

A similar approach is typically employed to determine a laser's linewidth by making one arm of an interferometer significantly longer than the other. When the optical path difference between the two arms exceeds the coherence length, the laser linewidth can be measured. In our situation, however, the goal is different. We are not interested in determining the linewidth; instead, we want to check whether there is a high-frequency noise background in the spectrum at the level of tens of MHz. For this purpose, a path difference of only 20 cm between the interferometer arms is sufficient.

I measured the spectra of the ALS seed, the Mephisto seed, and the amplifier when seeded with each of them (fig.3.13). As expected, there is a strong peak at 160 MHz, corresponding to the frequency shift introduced by the double-pass AOM. More importantly, the background noise levels differ significantly. The Mephisto shows the lowest background, the ALS level is about 10 dBm higher, and the amplifier output is another 7 dBm above that. Beyond 100 MHz the measured noise power appears to decrease, but this is likely due to the finite bandwidth of the photodiode.

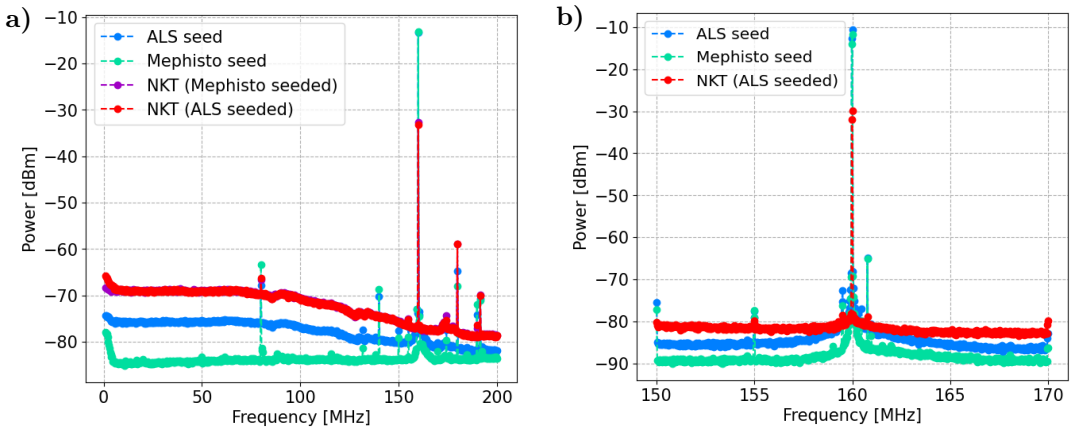


Figure 3.13: Recorded spectra of the beat signals on the photodiode with 3 kHz of resolution bandwidth (RBW). The baselines of the light coming out of the amplifier is 15 dBm higher than the Mephisto and 7 dBm from the ALS. After 100 MHz the the baselines seem to reduce, but it is probably due to the finite bandwidth of the photodiode. Panel (a) shows the full spectrum from 0 to 200 MHz, while panel (b) is a close up of 20 MHz of span centered around the beatnote frequency at 160 MHz.

Chapter 4

Photo-association spectroscopy

Photoassociation (PA) is the process by which two colliding atoms absorb a photon and are thereby converted into an electronically excited molecule. The development of laser-cooling techniques for producing ultracold atomic gases has made it possible to carry out photoassociation spectroscopy with exceptionally high spectral resolution [44]. PA spectroscopy allows one to probe the structure of both the electronically excited and the electronic ground-state interaction potentials.

One- and two-photon PA lines of ^{87}Rb–^{84,87,88}Sr had already been measured by our group on this apparatus [10], from which the interspecies s-wave scattering lengths of all these isotopologues could be determined (see Tab. 2.3). As discussed in Sec. 2.4, magnetoassociation of ^{87}Rb–^{84}Sr would be the most natural choice, but its extremely narrow Feshbach resonance makes association impractical. The isotopologue ^{87}Rb–^{87}Sr was therefore chosen as the next-best option, and the goal of this chapter is to measure PA lines for this pair of isotopes.

This chapter begins with a short introduction to photoassociation spectroscopy. I then describe how we reproduced some PA lines of ^{87}Rb–^{87,88}Sr with a partially different experimental setup, and discuss the benefits of reducing the dimensionality of the system using a 1D optical lattice. The chapter closes with a short discussion of the next steps, like two-photo PA spectroscopy and the coherent production of molecules in the electronic ground state.

4.1 Single photon PA spectroscopy

Consider a rubidium and a strontium atom, both in their electronic ground state, at large relative distance. The two atoms do not "see" each other, and the total energy of the system is simply the sum of the individual atomic energies, $E_{\mathrm{Rb}} + E_{\mathrm{Sr}}$, which we conveniently set to zero. As the atoms approach each other, they begin to interact via a molecular potential. In general, the exact shape of this potential depends upon the internal and external state of the atom pair.

If one of the two atoms – strontium, in our case – is instead in an electronically excited state, the pair interacts via a different, excited-state potential. Its large-distance asymptote is now the sum $E_{\mathrm{Rb}} + E_{\mathrm{Sr}^*}$, with strontium in the excited state; the energy difference between the two asymptotes is, as expected, the atomic transition energy $h\nu_{\mathrm{Sr}}$.

Each of these interaction potentials supports a number of discrete bound states,

which are the rovibrational levels of the RbSr dimer. Rather than exciting a single atom, one can instead excite the colliding *pair* of atoms directly into one of the bound levels of the excited-state potential (see fig.4.1). This process is called photoassociation (PA). In a single-photon PA process, two colliding atoms absorb a photon red-detuned from the atomic resonance by an amount Δ equal to the binding energy of the target excited molecular level, forming an excited molecule:

$$\mathrm{Rb} + \mathrm{Sr} + h\nu_{\mathrm{FB}} \rightarrow \mathrm{RbSr}^*.$$

We say that this photon drives the free-to-bound (FB) transition, and we refer to the corresponding laser as L_{FB}.

The excited molecule then decays, either back into free atoms or into a molecule bound in the electronic ground-state potential; both outcomes result in atom loss. Crucially, this decay is spontaneous and incoherent, so we have no control over its final state. By scanning the frequency of the PA laser and monitoring the remaining atom number in the trap, one maps out the spectrum of excited molecular levels.

The one-photon PA rate coefficient is [44]

$$K_{\mathrm{PA}} \propto |\langle \psi_\nu | \psi_k \rangle|^2, \tag{4.1}$$

where ψ_k is the continuum wavefunction describing the colliding atom pair at relative wavevector k, and ψ_ν is the wavefunction of the target rovibrational level ν of the excited-state potential. The squared overlap $|\langle \psi_\nu | \psi_k \rangle|^2$ is the free-bound Franck-Condon factor of the transition.

4.2 Two-photon PA spectroscopy

The structure of the electronic ground-state potential can be investigated by introducing a second photon that couples the rovibrational levels of the electronic ground state to those of the electronically excited state. Suppose the FB laser is held on resonance with a given atom-pair-to-excited-molecule transition, as described above. We then introduce a second laser, likewise detuned close to the Sr atomic transition. When this second laser is resonant with a ground-state-molecule-to-excited-molecule transition, it induces a light-shift on the excited molecular level, making the FB laser be off resonance so that it can no longer drive the FB transition. As a result, atom-pair to excited molecular level transition is suppressed and hence loss in atom number is suppressed, which means that more atoms are left in the trap. We say that this photon drives the bound-to-bound (BB) transition, and we refer to the corresponding laser as L_{BB}.

We define δ as the detuning between L_{BB} and L_{FB}:

$$\delta = \nu_{\mathrm{BB}} - \nu_{\mathrm{FB}} = \frac{E_{\mathrm{bind}}}{h}. \tag{4.2}$$

Note that δ directly gives the binding energy of the ground-state molecular level addressed by the BB laser.

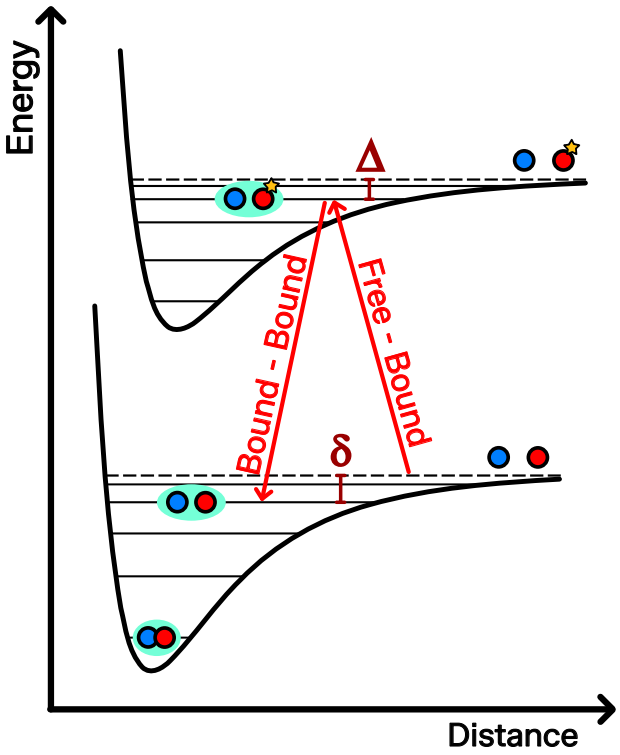


Figure 4.1: Level scheme of the photoassociation transitions. Two ground-state atoms (bottom) collide near the dissociation limit of the electronic ground-state potential and are photoassociated, via the free-bound (FB) laser, onto a rovibrational level of the excited-state potential, detuned by Δ from the atomic asymptote. A second, bound-bound (BB) laser couples the same excited level to a rovibrational level of the electronic ground-state potential. The two-photon detuning δ between the FB and BB lasers directly gives the binding energy of the addressed ground-state level.

4.3 Experimental setup for PA spectroscopy

During my master's project I built the optical setup for photoassociation spectroscopy. This setup must satisfy several constraints:

- the **linewidths** of L_{FB} and L_{BB} must be narrower than the linewidth of the excited state in order to resolve individual lines;
- the frequency of L_{FB} must be **red detuned** by few hundreds MHz from the ${}^1S_0 \rightarrow {}^3P_1$ transition of the isotope of Sr that we use. The frequency of L_{BB} must be **blue detuned** by few hundreds MHz from L_{FB};
- the relative phase noise between the two fields must be small, especially during the population-transfer pulse – a requirement that follows directly from energy-conservation arguments, since relative phase noise between the two lasers is equivalent to noise on the two-photon detuning δ;
- the positions of the PA lines are already known, but we still want to be able to **scan the frequency** by a few tens of MHz across each transition;
- the overlap between the scattering and molecular wavefunctions is generally very small, so we need as much **power** as possible. This is also relevant from a population-transfer point of view, since a large two-photon Rabi frequency is desirable there too;
- the experiment is already fairly complex and involves many lasers, so we want to keep this setup as **simple** and inexpensive as possible.

As shown in the following two sections, the solution that best satisfies all these constraints is an injection-locked laser, seeded with light (almost) resonant with the 689 nm atomic transition, combined with standard acousto-optic modulators (AOMs) to set the detunings.

Before building the setup, we still needed to choose the most favorable two-photon PA line for molecule production. Three lines were measured by our group [10] (see tab. 4.1). Since we want the largest possible two-photon Rabi frequency for the two-photon resonance, we chose the second transition; this choice also fixed the AOM center frequencies used below (350 MHz and 150 MHz), which double-pass to roughly Δ and δ of this line, respectively.

Δ	δ	Transition	$\Omega/2\pi$ (kHz/$\sqrt{\mathrm{mW/cm^2}}$)
686.79(23)	199.97(17)	σ^-	6.0(5)
686.79(23)	287.27(18)	σ^-	22.2(2.0)
686.79(23)	1950.24(11)	σ^-	–

Table 4.1: Results of two-color PA spectroscopy of ^{87}Rb–^{87}Sr, from [10]. Δ is the detuning in MHz of L_{FB} from the ${}^1S_0(F = 9/2) \rightarrow {}^3P_1(F' = 11/2)$ transition of ^{87}Sr. δ is the detuning in MHz of L_{BB} from L_{FB}, which corresponds to the binding energy $h\delta$ of the molecule. The column labeled "Transition" shows the type of transition addressed by both L_{FB} and L_{BB}. The last column gives the bound-bound Rabi frequencies, where measured. Adapted from [10].

4.3.1 Injection locked laser

To achieve sufficient power and narrow linewidth, we use an injection-locked diode laser (ILL). The diode is a Fabry-Perot (FP) diode (Ushio HL69001DG), housed in a Toptica DL100 laser head without external cavity. The injection light comes from the red-spider system, resonant with the $^1S_0(F = 9/2) \rightarrow {}^3P_1(F' = 11/2)$ transition of ^{87}Sr, and is sent into the diode through an optical isolator (see Fig. 4.4). The master frequency is set via an AOM to be 20 MHz detuned from the red Sr transition, to ensure that no resonant light is shone on the atoms. The light amplified by the injection-locked diode inherits the spectral properties of the master laser, while providing 150 mW of output power from as little as 240 μW of seed power. The locking quality is monitored via the transmission signal of an FP cavity.

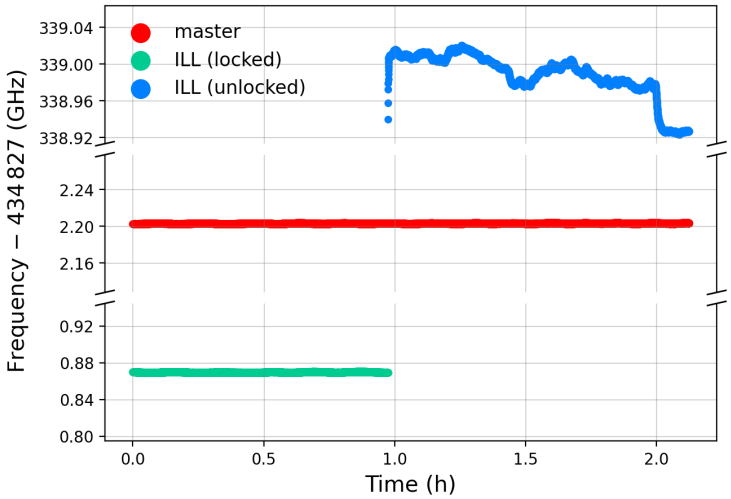


Figure 4.2: Wavemeter traces of the master laser (red) and the injection-locked laser (ILL), with (green) and without (blue) injection. When the seed light from the master is blocked, the free-running ILL diode fluctuates by roughly 100 MHz over about one hour, whereas when it is injected, its stability matches that of the master. Note that the master frequency sent to the wavemeter is resonant with the $^1S_0 \rightarrow {}^3P_1$ transition of ^{88}Sr, while the injection frequency is picked off after a series of AOMs that make it just 20MHz detuned from the $^1S_0(F = 9/2) \rightarrow {}^3P_1(F' = 11/2)$ transition of ^{87}Sr.

An important property of ILLs is the so-called injection bandwidth: the range of seed frequencies over which the ILL can be injected and remain properly locked. This interval is generally not symmetric around the injection frequency and depends on several parameters, such as the diode type, the gain-medium material, the linewidth enhancement factor, the injection power, and the temperature [45].

Ideally, one wants the amplifying device to simply amplify any injected light, i.e., to have the largest possible injection bandwidth. Amplifiers based on a simple gain medium, such as tapered amplifiers (TAs), can produce watt-level output power with an efficiency limited only by the bandwidth of the gain medium. We decided against using a TA for three main reasons. First, TAs are considerably more expensive and fragile than FP diodes. Second, we currently have only a few hundred μW of seed light available from the main 689 nm setup, whereas a TA would require several mW to seed properly. Third, we do not expect to need watt-level power to drive the FB

and BB transitions: we hope that confinement-induced resonances will allow us to reach adequate two-photon Rabi frequencies with more modest power. Similarly, anti-reflection (AR)-coated diodes are less wavelength-selective – and hence support a broader injection bandwidth – than FP diodes, but they are more expensive. As we will see in Sec. 4.4, the injection bandwidth we obtain with the FP diode is large enough to scan a few tens of MHz across the PA lines.

Injection bandwidth and temperature dependence.

To find the diode temperature that gives the largest injection bandwidth, I characterized the ILL at several temperatures. Let us first set the temperature dependence aside and describe the characterization method itself.

The AC modulation port on the laser control module allows the diode current to be modulated with an external function generator. Changing the diode current has two main effects: the optical output power, approximately proportional to the current, follows the modulation; and the emission frequency of the diode also shifts with current. Figure 4.3a shows the output voltage of a photodiode (PD), directly proportional to the optical power, as a function of diode current, without injection.

If the seed light is allowed into the diode, the diode gets injected over a certain range of currents; within this range, the seed lowers the diode's effective lasing threshold, so the output power increases slightly at the lock point. This situation is shown in Fig. 4.3b.

Let's now consider the effect of the temperature. Figure 4.3a shows that, at fixed current, the output power *increases* with diode temperature. Interestingly, once injection is allowed, the peaks reach different heights *relative to their own background*, but in such a way that their *absolute* height is the same at every temperature (Fig. 4.3b). This set of temperatures has been chosen such that the injection peak occurs always at approximately the same current in order to be able to compare them.

Figure 4.3c shows the temperature dependence of the width of the injection (locking) range. At lower temperatures the plateau region becomes wider, i.e., the injection bandwidth increases. The absolute optical power is the same for all the peaks, even though the baselines differ in height. This might suggest that the seed light pulls the effective lasing threshold current to the same value at every temperature, yielding equal output powers at equal diode currents.

For low seed powers, the locking range scales approximately as [45]

$$\Delta\omega_{\text{lock}} \propto \sqrt{\frac{P_{\text{seed}}}{P_{\text{ILL}}}}\,, \tag{4.3}$$

but as the injection power increases, instabilities can arise: the laser dynamics can, for example, undergo limit-cycle oscillations, multi-mode emission, and even chaotic behavior [46]. Experimentally, I observed that, starting from low injection power, the injection peak first appears and grows to its maximum height; it then turns into a plateau resembling a square pulse. If the injection power is increased further beyond a certain value, the peak begins to deform and side peaks appear. The injection power required to reach the widest locking range, just before these side features appear, is shown in Fig. 4.3d. Even though this method remains fairly qualitative, it clearly shows the dependence of the saturation power on temperature.

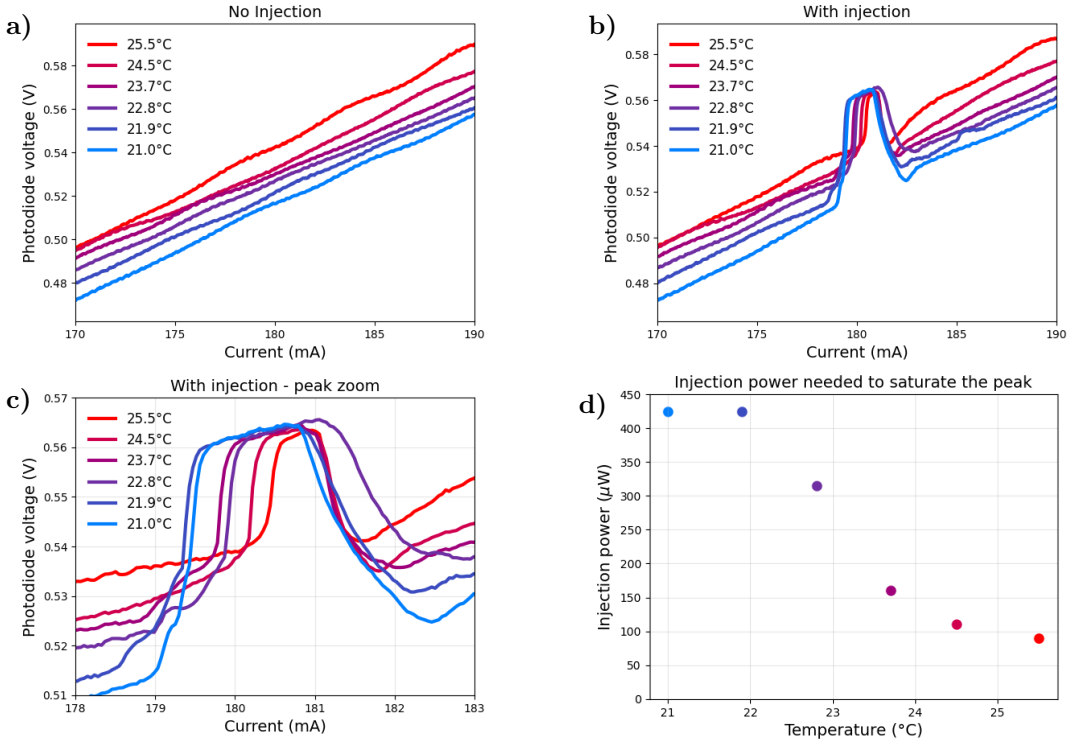


Figure 4.3: Injection-locked laser behavior at different temperatures. The diode current is modulated via the AC modulation port on the laser control module, using a triangular waveform of 20 mA peak-to-peak amplitude at 10 Hz (only half a period is shown here). The optical power is recorded with a commercial photodiode. (a) Without seed light, the power is directly proportional to the diode current. (b) Over a range of currents, the seed light lowers the effective lasing threshold and the output power increases. (c) The current interval over which the diode is injected – the injection bandwidth – has a width that depends on temperature. (d) The seed power needed to saturate the injection peak (see text) is inversely proportional to temperature. We stopped at 21 °C because the available seed power was not sufficient to saturate the peak.

In summary, lower diode temperatures yield a wider locking range, provided the injection power is increased accordingly. For this reason we chose to operate the diode at 22 °C, the lowest temperature at which we can still drive the injection peak close to saturation with the available seed power – reasonable also from the point of view of a gain-medium amplifier, since operating close to saturation is generally desirable for a more stable output. Moreover, at fixed injection power the plateau does not appear to widen appreciably below this temperature (see Fig. 4.3d, the points at 21 and 21.9 °C have the same same injection power – the maximum available – and the peaks width is the same).

The resulting locking bandwidth of $\approx 1.5\,\mathrm{mA}$ corresponds to roughly 30 MHz. As mentioned before, one- and two-photon PA lines had already been measured by our group some years ago [47, 10]. They used a different setup, based on a laser locked via a beatnote with a sideband of the master laser, generated with a sideband generator. This allowed them to scan continuously from the Sr atomic transition up to 10 GHz to the red. Since we already know the position of the PA lines, our scan range is wide enough.

4.3.2 Optical setup

The optical setup I built is shown in Fig. 4.4. It is split across two breadboards: one where the light is generated, and one where it is detuned to reach the PA transitions.

On the first breadboard, a fiber carries 689 nm light from the red-spider system to seed the ILL. The quality of the injection is monitored by recording the transmission through an FP cavity with a photodiode. A second fiber brings a few hundred μW of light to the wavemeter, to monitor the absolute frequency of the amplified light. About 96 mW of light are coupled into the fiber connecting the two breadboards.

The second breadboard hosts two double-pass AOMs. The first, with a central frequency of 350 MHz, shifts the light to the red of the Sr $^1S_0 \rightarrow {}^3P_1$ atomic transition (using the -1 diffraction order) by Δ; this light drives the FB transition. About half of it is coupled into the fiber going to the experiment. The other half is shifted, by the second double-pass AOM (center frequency 150 MHz), to the blue ($+1$ order) by δ; this light drives the BB transition. We overlap the two PA components on a non-polarizing 50:50 beam splitter (BS), since they must share the same polarization, and couple the combined light into a single-mode fiber that goes to the experiment. On the experimental table, the polarization is converted from linear to circular and the light is focused to 150 μm on the atoms.

Recall that the injection (seed) light is deliberately detuned by 20 MHz from the Sr transition, to avoid having any resonant light present in the system: resonant light reaching the atoms would be highly undesirable, since we interpret atom loss as a photoassociation signal.

For single-photon PA spectroscopy, we often scan the frequency of the seed light itself rather than the AOM on the second breadboard, since – far from the AOM's central frequency – its finite bandwidth and diffraction efficiency start to noticeably affect the diffracted power. By instead scanning the seed frequency, we obtain the same optical power out of the diode at every point of the scan, as long as the ILL remains properly locked.

If more optical power is needed, a few modifications to the setup are possible. For example, the fiber connecting the two breadboards is practically convenient, but

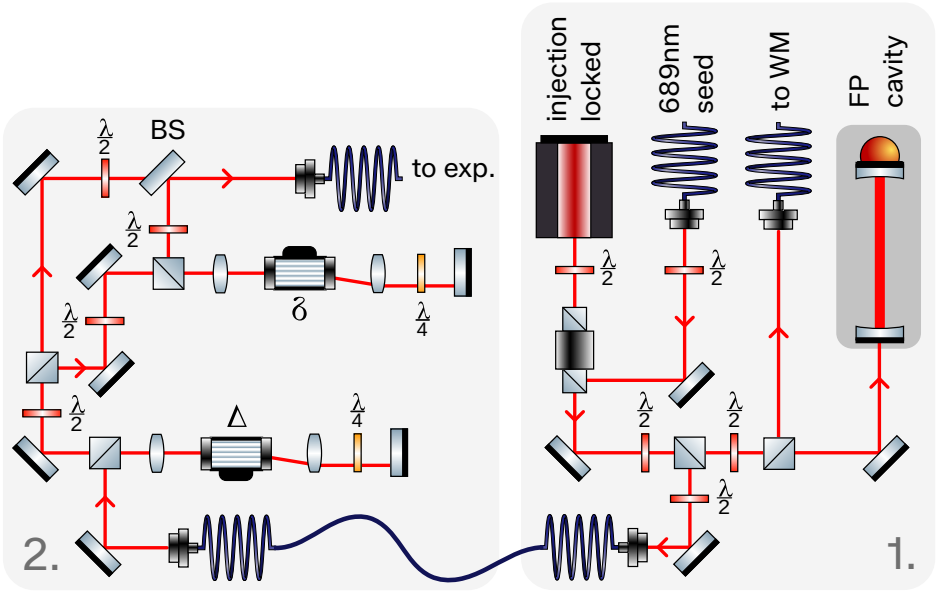


Figure 4.4: Schematic of the PA optical setup, split across two breadboards. Breadboard 1 (right) houses the injection-locked laser: the FP diode is seeded with 689 nm light, its injection quality is monitored via the transmission of an FP cavity, and its output frequency is checked with a wavemeter (WM). Breadboard 2 (left) contains the two double-pass AOMs generating the FB (Δ) and BB (δ) components, which are recombined on a non-polarizing 50:50 beam splitter (BS) and coupled into the fiber that goes to the experiment.

its finite coupling efficiency causes some power loss. Another point worth revisiting is that the light for the second photon currently passes through the first AOM as well: this arrangement makes the estimate of the binding energy straightforward, since it is simply given by δ, but it wastes power, as each additional AOM pass introduces its own diffraction loss.

4.4 One-photon spectroscopy results

In this section I report the details and results of the one-photon PA spectroscopy. Measurements were performed with both ^{88}Sr and ^{87}Sr. Although the fermionic isotope is our candidate for molecule production, it is much more challenging to measure PA signals with it, due to strong three-body losses with Rb. Working with the bosonic isotope is much simpler, and allowed us to first test the setup.

Since the positions of the PA lines are already known, we do not need to search for them, but only need to optimize the sample conditions to maximize the contrast. We prepare the mixture as described in Sec. 2.5, illuminate it with the FB laser, and measure the surviving Rb atom number as a function of laser frequency. A resonance appears as a dip in the atom number, whose depth and width depend on the laser intensity, the pulse duration, and the Franck-Condon overlap with the initial scattering state. Since the PA frequency is close to the Sr atomic transition, we monitor Rb rather than Sr, to make sure that the observed losses are due to molecule formation and not to off-resonant atomic scattering.

4.4.1 PA spectroscopy of ^{87}Rb–^{88}Sr

We started our search for PA lines with the ^{87}Rb–^{88}Sr combination, since working with ^{88}Sr is simpler than ^{87}Sr from many points of view. The experimental sequence is considerably shorter: it is reduced by about 10 s, since the MOT loading and additional cooling steps needed for ^{87}Sr are no longer required. These steps are slow because of the low natural abundance of the fermionic isotope, combined with the reduced cooling efficiency arising from its nonzero nuclear spin. ^{88}Sr, in contrast, is the most abundant isotope and has no hyperfine structure. We also skip the delicate steps of transporting the lower trap along the dimple and merging it with the lattice, which is a significant advantage, since the atoms are very fragile close to degeneracy and these steps otherwise require fine, near-daily optimization.

Another advantage of working with the bosonic isotope is that the mixture with Rb is stable: it exhibits no strong inter-species loss channel, so we can reach higher densities – a very relevant parameter for photoassociation, since it increases the probability that atoms collide and scatter a PA photon.

We selected PA lines from [47], Tab. 5.2, chosen such that they could be easily reached with the AOM combination in our setup. The injection light was resonant with the $^1S_0 \to {}^3P_1$ transition of ^{88}Sr, which I will denote ν_{88}, shifted by +80 MHz. Taking into account the center frequencies of the double-pass AOMs in the PA setup, this gives

$$\nu_{88} + 80\,\mathrm{MHz} - (2 \times 350\,\mathrm{MHz}) + (2 \times 150\,\mathrm{MHz}) = \nu_{88} - 320\,\mathrm{MHz},$$

and there are 7 lines between −260 MHz and −364 MHz, all within reach given the AOM bandwidth. We measured the first 4 of them, using between 1.4 and 2.4 mW of power for 1 to 2 s, with a beam waist of 110 μm. Figure 4.5 shows the measurements, and Table 4.2 reports the fit results, compared with the previous results from our group.

measured Δ	measured FWHM	tabulated Δ	tabulated FWHM
260.62(1)	0.42(2)	260.54(5)	1.33(17)
265.62(1)	0.47(4)	265.58(5)	1.57(61)
273.00(2)	0.75(7)	272.91(7)	0.86(52)
326.98(2)	0.52(7)	326.93(4)	1.80(20)

Table 4.2: Results of single-photon photoassociation spectroscopy of ^{87}Rb–^{88}Sr with our setup, compared with the values tabulated in [47], Tab. 5.2 (in MHz). The detuning Δ is referenced to the $^1S_0 \to {}^3P_1$ transition of ^{88}Sr; the absolute transition frequency is $\nu_{88} - \Delta$. The measured line positions agree with the previous measurements, while the linewidths of transitions 1, 2 and 4, estimated as FWHM, are roughly a factor of 3 narrower.

The contrast lies between 70% and 80%, with low noise. The line positions are compatible with the previous measurements, while the linewidths of transitions 1, 2 and 4, measured as FWHM, are roughly a factor of 3 narrower. We can therefore conclude that our setup reproduces the earlier results well, and move on to ^{87}Rb–^{87}Sr.

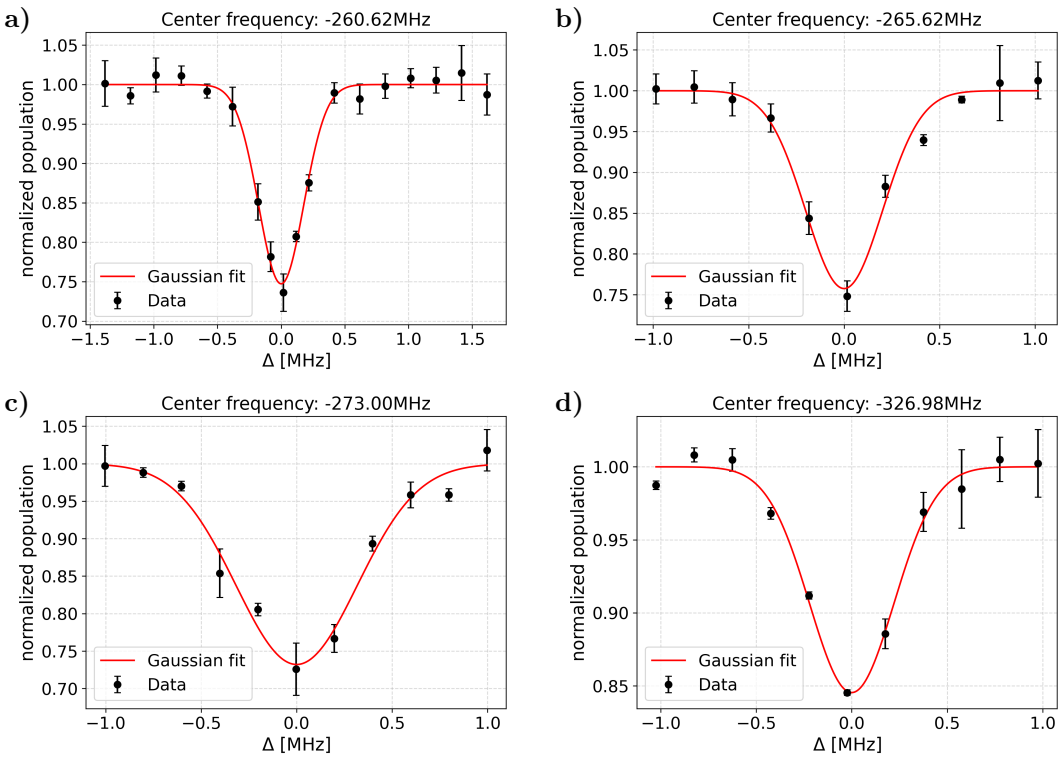


Figure 4.5: Measurements of single-photon photoassociation transitions for ^{87}Rb–^{88}Sr (in MHz). The fitted center of each transition is given above the corresponding panel, referenced to the $^1S_0 \rightarrow {}^3P_1$ transition of ^{88}Sr. The x-axis shows the frequency scan range, and the y-axis shows the Rb atom number, normalized to the fitted baseline value.

4.4.2 PA spectroscopy of ^{87}Rb–^{87}Sr

PA spectroscopy of the ^{87}Rb–^{87}Sr mixture is particularly challenging, owing mainly to the large interspecies scattering length, which causes atom loss even without illuminating the sample with the PA beams. This forces us to work at lower densities, which in turn reduces the probability of two atoms colliding. Moreover, compared to ^{87}Rb–^{88}Sr, the experimental sequence is longer, due to the loading and cooling of ^{87}Sr, and more complex, due to the transport and merging stages. The presence of ten hyperfine states makes the laser cooling procedure less efficient. Finally, evaporative cooling is ineffective, since polarized fermions interact predominantly via p-wave collisions.

Conscious of these difficulties, we spent a lot of time optimizing the samples conditions until we were able to measure the targeted PA line (the one at $\delta = 287.27\,\mathrm{MHz}$ in Table 4.1). We shine few mW of light for 500-1000 ms. We run the fast coils at 2 A, which corresponds to a magnetic field of 2.12 G [24]. We were also able to exploit an additional tool: the optical lattice. Figure 4.6 shows the PA measurements with and without the lattice. Without the lattice, the measurement is very noisy and the feature barely emerges above the background; here we illuminate the sample with the PA beam for 1000 ms at $\approx 20\,\mathrm{mW}$ of power. With the lattice, we can instead illuminate for only 500 ms at the same power, and obtain both better contrast and lower noise.

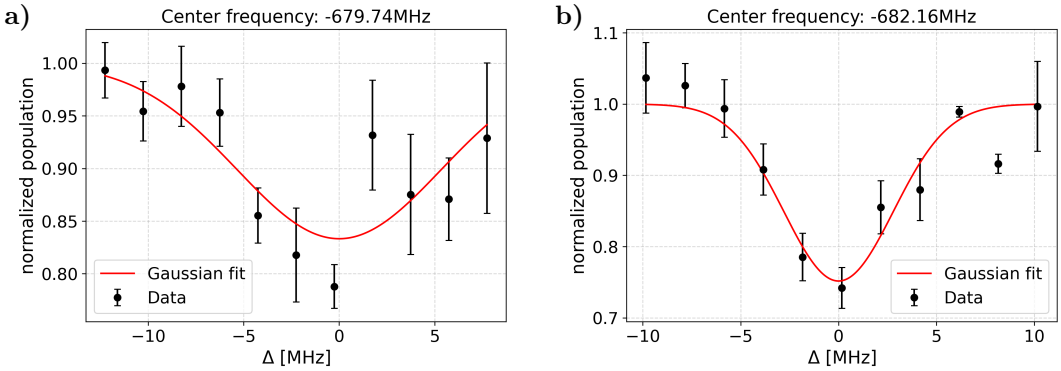


Figure 4.6: Measurements of the single-photon photoassociation transition for ^{87}Rb–^{87}Sr (in MHz). The fitted center of the transition is given above each panel, referenced to the $^1S_0(F = 9/2) \rightarrow {}^3P_1(F' = 11/2)$ transition of ^{87}Sr. The x-axis shows the frequency scan range, and the y-axis shows the Rb atom number, normalized to the fitted baseline value. (a) Without the lattice the feature is very noisy and wide. (b) with the lattice we can shine the PA beam for half the time and get a much cleaner and narrower feature.

The magnetic shift of this molecular level has been estimated in [47](tab.5.3) to be -1.61(1) MHz/G. In our case it corresponds to a shift of -3.41 MHz. In tab.4.3 I report the position of the PA line at zero field.

This improvement in signal quality comes from two effects of the lattice. The first is the stabilization of the mixture, which yields a colder sample and a more reproducible background. The second is the higher density, which increases the collision rate and allows us to halve the illumination time. This is not yet a confinement-induced resonance, as a true CIR should enhance the wavefunction overlap by a much larger factor.

dimensionality	Δ	FWHM
3D	683(1)	13(6)
2D	685.6(4)	6.6(1.3)

Table 4.3: Results of single-photon photoassociation spectroscopy of ^{87}Rb–^{87}Sr (in MHz) at zero field, without (3D) and with (2D) the 1D optical lattice. The frequency discrepancy between the two measurements lies well within one standard deviation of the fitted gaussians and can be attributed to the noise in the data points. The tabulated value of 686.79(23) in tab. 4.1 falls well within one standard deviation.

4.5 Next steps

In this section I briefly outline the next steps to be pursued, such as carry out two-photon spectroscopy and implement a second optical lattice, along with ideas for the future.

Two-photon PA spectroscopy. When atoms get excited by L_{FB}, they populate a molecular electronic-excited state. This state can decay either back to a scattering state or to a molecular state in the electronic groundstate manifold. Both are incoherent processes and result in particles loss. A way to solve this problem is to couple the electronic-excited state to the electronic-ground state by a second laser, namely L_{BB}. Finding a molecular electronic-ground state with a good overlap with the electronic-excited state is essential for having an efficient population transfer. As mentioned before, we already have a candidate from 4.1. While writing this thesis, measurements of two-photon PA spectroscopy are being carried out.

Second lattice implementation. A confinement-induced resonance (CIR) would allow scattering atom pairs to be transferred directly into the first weakly bound state of the electronic ground-state manifold. As mentioned in Sec. 3.1.2, this would enhance the wavefunction overlap by several orders of magnitude, greatly increasing the FB transition Rabi frequency. While there are hints that a CIR might occur already in a quasi-2D confinement, our theory collaborators at UvA have shown, in a dedicated paper, that a CIR does exist in a genuinely 1D geometry [11]. It would therefore be well worth aligning a second lattice onto the atoms to try to exploit this effect.

Coherent population transfer with STIRAP The ultimate goal of the experiment is not merely to probe the molecular states, but to produce molecules in the electronic ground state. Rather than simply driving the molecular resonance and measuring loss, we want to perform coherent population transfer. The theory of three-level systems can be found in [48], Ch. 6.

Stimulated Raman adiabatic passage (STIRAP) is a coherent population transfer technique that transfers population between two states $|1\rangle$ (atom pair continuum) and $|3\rangle$ (ground-state molecule) via an intermediate excited state $|2\rangle$ (excited molecule), without ever populating $|2\rangle$ and therefore without spontaneous emission losses. The system is described by the three-level Hamiltonian in the rotating wave

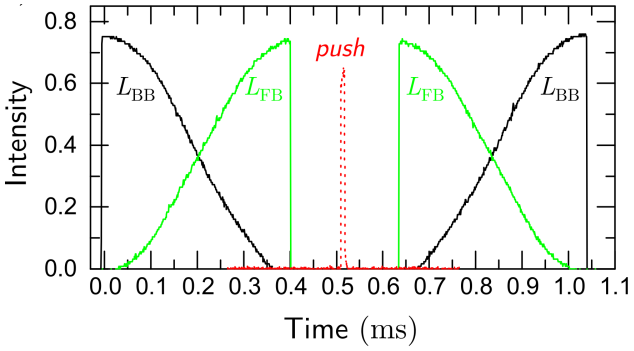


Figure 4.7: Counterintuitive STIRAP pulse sequence: the Stokes (BB) pulse precedes and partially overlaps the pump (FB) pulse. To quantify the efficiency of the process, the STIRAP pulses are followed by a *push* pulse resonant with an atomic transition. Atoms that have not undergone association are expelled from the trap by this push pulse, whereas atoms that have formed bound molecular states remain confined. Subsequently, a reversed STIRAP pulse sequence is applied to transfer the molecules back into single-atom states, which are then detected via imaging. By comparing the initial number of atoms with the final number of atoms that remain after the complete STIRAP–push–STIRAP sequence, the efficiency of a single STIRAP transfer can be inferred. Figure adapted from [47].

approximation [49]:

$$H = -\frac{\hbar}{2}\begin{pmatrix} 0 & \Omega_{\mathrm{FB}}(t) & 0 \\ \Omega_{\mathrm{FB}}(t) & 2\Delta_{\mathrm{FB}} & \Omega_{\mathrm{BB}}(t) \\ 0 & \Omega_{\mathrm{BB}}(t) & 2(\Delta_{\mathrm{FB}} - \Delta_{\mathrm{BB}}) \end{pmatrix}, \tag{4.4}$$

where $\Omega_{\mathrm{FB}}(t)$ and $\Omega_{\mathrm{BB}}(t)$ are the time-dependent Rabi frequencies of the pump and Stokes fields, and Δ_{FB}, Δ_{BB} are the corresponding single-photon detunings. On two-photon resonance ($\Delta_{\mathrm{FB}} = \Delta_{\mathrm{BB}}$), the Hamiltonian has a dark eigenstate

$$|D\rangle = \cos\theta(t)|1\rangle - \sin\theta(t)|3\rangle, \qquad \tan\theta(t) = \frac{\Omega_{\mathrm{FB}}(t)}{\Omega_{\mathrm{BB}}(t)} \tag{4.5}$$

which is decoupled from $|2\rangle$ for any mixing angle $\theta(t)$. By applying the Stokes (BB) pulse *before* the pump (FB) pulse (counterintuitive pulse ordering), the system is initialized in $|D\rangle \equiv |1\rangle$, since $\Omega_{\mathrm{FB}} \to 0$ initially implies $\theta \to 0$. As the pulses overlap, and Ω_{FB} grows while Ω_{BB} decreases, θ rotates adiabatically from 0 to $\pi/2$, transferring the population entirely into $|3\rangle$ without any transient occupation of $|2\rangle$.

The Rabi frequency of the effective 2-level system is:

$$\Omega_{\mathrm{R}} = \frac{\Omega_{\mathrm{BB}}\Omega_{\mathrm{FB}}}{2\Delta}. \tag{4.6}$$

At the same time, there is an effective residual decay rate from the population that still leaks into the excited state:

$$\Gamma_{\mathrm{eff}} = \Gamma_{\mathrm{nat}}\,\frac{\Omega_{\mathrm{BB}}^2 + \Omega_{\mathrm{FB}}^2}{4\Delta^2}. \tag{4.7}$$

The different scaling of Ω_{R} and Γ_{eff} with Δ shows that, at large detuning, off-resonant scattering from the excited state becomes much weaker. The price to pay

is a smaller Rabi frequency, which we try to compensate for by using as much optical power as possible.

The adiabaticity condition requires [49]:

$$\dot{\theta} \ll \frac{\sqrt{\Omega_{\mathrm{FB}}^2 + \Omega_{\mathrm{BB}}^2}}{2} \tag{4.8}$$

which in practice demands peak Rabi frequencies large compared to $1/T$, where T is the pulse duration. The transfer efficiency is limited in practice by the decoherence rate of the two-photon transition, set by the relative laser linewidth and by the finite lifetime of the atoms in the trap.

Exploring other manifolds. So far, PA spectroscopy of RbSr has been carried out near the $^1S_0 \to {}^3P_1$ transition of Sr at 689 nm. This was the most natural choice, since a narrow-linewidth laser was already available. There is also the $^1S_0 \to {}^1P_1$ transition near 461 nm, which has a much larger natural linewidth, around 30 MHz, so that the molecular levels built on this asymptote are also expected to be broad. This does not necessarily mean that the corresponding PA transitions are easy to drive (i.e., that they have a large Rabi frequency); if anything, the larger linewidth could make STIRAP *less* efficient, owing to increased spontaneous-emission losses from the excited state. Nevertheless, this manifold could still be worth investigating further. Similarly, Rb transitions could be explored, starting from the usual D_2 line and moving toward less common transitions.

Feshbach resonance from metastable state. Another idea is to pump Sr into the metastable $^3P_2$ state, which has a lifetime of ≈ 500 s. In this state, Sr is magnetic, and Feshbach resonances might become accessible [50]. This, however, amounts to a rather different experiment, and it would take considerable time even to assess its feasibility.

Chapter 5

Conclusions and outlook

The goal of the RbSr experiment is the production of ultracold RbSr molecules in the electronic ground state. Since the Feshbach resonances between an alkali and a closed-shell atom are far too narrow to be used for magnetoassociation, the route we follow is optical association of a ^{87}Rb–^{87}Sr pair, assisted by the tight confinement of an optical lattice. The work presented in this thesis addresses two of the ingredients this route requires: a working one-dimensional optical lattice, and a laser system able to drive the free-bound and bound-bound molecular transitions.

The first part of the work concerns the 1D optical lattice. Both parametric heating and Kapitza-Dirac diffraction of a Rb BEC returned lattice depths of about 20% of the calculated value, and the fact that two independent methods agreed with each other pointed at the lattice itself rather than at the measurement. A sequence of center-of-mass oscillation measurements showed that power, waist, polarization and alignment were all as expected, leaving the coherence of the light as the only remaining suspect. To test it I built a small portable interferometer based on a lateral displacement prism, which measures the fringe visibility of any laser source from a few mW delivered through a fiber. The old amplifier yielded a visibility of 21%, against 87% for a new unit of the same model and seed, and a Michelson beatnote measurement confirmed the presence of a broadband phase-noise background in its emission spectrum. Replacing the amplifier restored close to the expected lattice frequencies.

During my project I built the optical setup for photoassociation spectroscopy. The core of it is an injection-locked Fabry-Perot diode seeded with a few hundred μW of 689 nm light from the main red laser system, which delivers 150 mW while inheriting the sub-kHz linewidth of the master – a solution that is cheap and effective. I characterized the injection bandwidth as a function of diode temperature and seed power, and found that a lower temperature widens the locking range provided the seed power is increased accordingly; operating at 22 °C gives a locking range of about 30 MHz, wide enough to scan across the known photoassociation lines. Two double-pass acousto-optic modulators, at 350 MHz and 150 MHz, then generate the free-bound and bound-bound components with the detunings required by the target two-photon line, and recombine them into a single fiber going to the experiment.

With a working lattice we could demonstrate its two intended uses. First, confining the ^{87}Rb–^{87}Sr mixture to a quasi-two-dimensional geometry suppresses the three-body recombination that otherwise makes this resonantly interacting mixture

short-lived: we observe a fairly sharp crossover around a Sr lattice frequency of 20 kHz, beyond which the mixture survives for several hundred milliseconds without significant heating. Second, we used the lattice as a tool for spectroscopy. After reproducing four known one-photon photoassociation lines of ^{87}Rb–^{88}Sr, in agreement with the previous measurements of our group and with linewidths about a factor of three narrower, we measured the target ^{87}Rb–^{87}Sr line. Without the lattice the feature barely emerges from the noise; with the lattice, half the illumination time is enough to obtain a much cleaner resonance, whose width drops from 13 to 6.6 MHz. This gain comes from the stabilization and the increased density of the confined sample rather than from a confinement-induced resonance, which would enhance the free-bound overlap by a much larger factor.

The natural continuation is already under way. Two-photon spectroscopy of ^{87}Rb–^{87}Sr is being performed while this thesis is written, and will give the binding energy of the ground-state level we intend to populate. Aligning a second lattice beam onto the atoms would produce the quasi-1D confinement in which a confinement induced resonance has been predicted for this isotopologue. With both photons available and the molecular levels located, the remaining step is coherent population transfer by stimulated Raman adiabatic passage, which would yield RbSr molecules bound by more than 200 MHz (in frequency units). A second STIRAP step would then be all that is needed to finally deliver RbSr molecules in the electronic ground state

Bibliography

[1] G. Baroni, C. Lamporesi and M. Zaccanti. Quantum mixtures of ultracold gases of neutral atoms. *Nature Reviews Physics*, 6, Dec 2024.

[2] Immanuel Bloch, Jean Dalibard, and Wilhelm Zwerger. Many-body physics with ultracold gases. *Rev. Mod. Phys.*, 80:885–964, Jul 2008.

[3] Yewei Wu, Justin J. Burau, Kameron Mehling, Jun Ye, and Shiqian Ding. High phase-space density of laser-cooled molecules in an optical lattice. *Phys. Rev. Lett.*, 127:263201, Dec 2021.

[4] Luigi De Marco, Giacomo Valtolina, Kyle Matsuda, William G. Tobias, Jacob P. Covey, and Jun Ye. A degenerate fermi gas of polar molecules. *Science*, 363(6429):853–856, 2019.

[5] Niccolò Bigagli, Weijun Yuan, Siwei Zhang, Boris Bulatovic, Tijs Karman, Ian Stevenson, and Sebastian Will. Observation of bose–einstein condensation of dipolar molecules. *Nature*, 631(8020):289–293, June 2024.

[6] Barbé Vincent. *Ultracold RbSr: Optical and magnetic spectroscopy, Feshbach resonances and molecular structure.* PhD thesis, Universiteit van Amsterdam, 2020.

[7] Piotr S. Żuchowski, J. Aldegunde, and Jeremy M. Hutson. Ultracold rbsr molecules can be formed by magnetoassociation. *Phys. Rev. Lett.*, 105:153201, Oct 2010.

[8] Vincent Barbé, Alessio Ciamei, Benjamin Pasquiou, Lukas Reichsöllner, Florian Schreck, Piotr S. Żuchowski, and Jeremy M. Hutson. Observation of feshbach resonances between alkali and closed-shell atoms. *Nature Physics*, 14(9):881–884, June 2018.

[9] Alex Bayerle. *Ultracold strontium and rubidium: mixtures, quantum gases and molecules.* PhD thesis, Universiteit van Amsterdam, 2017.

[10] Alessio Ciamei, Jacek Szczepkowski, Alex Bayerle, Vincent Barbé, Lukas Reichsöllner, Slava M. Tzanova, Chun-Chia Chen, Benjamin Pasquiou, Anna Grochola, Pawel Kowalczyk, Wlodzimierz Jastrzebski, and Florian Schreck. The rbsr $2\sigma^+$ ground state investigated via spectroscopy of hot and ultracold molecules. *Phys. Chem. Chem. Phys.*, 20:26221–26240, 2018.

[11] Lorenzo Oghittu, Premjith Thekkeppatt, Nirav P. Mehta, Seth T. Rittenhouse, Klaasjan van Druten, Florian Schreck, and Arghavan Safavi-Naini. Confinement-induced resonances for the creation of quasi-one-dimensional ultracold gases of alkali–alkaline-earth dimers. *Physical Review A*, 112(4), October 2025.

[12] Simon L. Cornish, Michael R. Tarbutt, and Kaden R. A. Hazzard. Quantum computation and quantum simulation with ultracold molecules. *Nature Physics*, 20(5):730–740, May 2024.

[13] Lincoln D Carr, David DeMille, Roman V Krems, and Jun Ye. Cold and ultracold molecules: science, technology and applications. *New Journal of Physics*, 11(5):055049, may 2009.

[14] V. Andreev, D. G. Ang, D. DeMille, J. M. Doyle, G. Gabrielse, J. Haefner, N. R. Hutzler, Z. Lasner, C. Meisenhelder, B. R. O'Leary, C. D. Panda, A. D. West, E. P. West, X. Wu, and ACME Collaboration. Improved limit on the electric dipole moment of the electron. *Nature*, 562(7727):355–360, October 2018.

[15] Tanya S. Roussy, Luke Caldwell, Trevor Wright, William B. Cairncross, Yuval Shagam, Kia Boon Ng, Noah Schlossberger, Sun Yool Park, Anzhou Wang, Jun Ye, and Eric A. Cornell. An improved bound on the electron's electric dipole moment. *Science*, 381(6653):46–50, July 2023.

[16] Alessio Ciamei, Adam Koza, Marcin Gronowski, and Michał Tomza. Ultracold high-spin σ-state polar molecules for new physics searches. *Physical Review X*, 16(1), March 2026.

[17] Timo Fleig and David DeMille. Theoretical aspects of radium-containing molecules amenable to assembly from laser-cooled atoms for new physics searches. *New Journal of Physics*, 23(11):113039, November 2021.

[18] Tijs Karman, Michał Tomza, and Jesús Pérez-Ríos. Ultracold chemistry as a testbed for few-body physics. *Nature Physics*, 20(5):722–729, May 2024.

[19] Tim Langen, Giacomo Valtolina, Dajun Wang, and Jun Ye. Quantum state manipulation and cooling of ultracold molecules. *Nature Physics*, 20(5):702–712, May 2024.

[20] Tijs Karman and Jeremy M. Hutson. Microwave shielding of ultracold polar molecules. *Phys. Rev. Lett.*, 121:163401, Oct 2018.

[21] Simon Stellmer, Meng Khoon Tey, Bo Huang, Rudolf Grimm, and Florian Schreck. Bose-einstein condensation of strontium. *Phys. Rev. Lett.*, 103:200401, Nov 2009.

[22] Simon Stellmer, Meng Khoon Tey, Rudolf Grimm, and Florian Schreck. Bose-einstein condensation of ^{86}Sr. *Phys. Rev. A*, 82:041602(R), Oct 2010.

[23] Meng Khoon Tey, Simon Stellmer, Rudolf Grimm, and Florian Schreck. Double-degenerate bose-fermi mixture of strontium. *Phys. Rev. A*, 82:011608(R), Jul 2010.

[24] Simon Stellmer. *Degenerate quantum gases of strontium*. PhD thesis, University of Innsbruck, 2012.

[25] Mateusz Borkowski, Lukas Reichsöllner, Premjith Thekkeppatt, Vincent Barbé, Tijs van Roon, Klaasjan van Druten, and Florian Schreck. Active stabilization of kilogauss magnetic fields to the ppm level for magnetoassociation on ultranarrow feshbach resonances. *Review of Scientific Instruments*, 94(7):073202, 07 2023.

[26] Caroline L. Blackley, C. Ruth Le Sueur, Jeremy M. Hutson, Daniel J. McCarron, Michael P. Köppinger, Hung-Wen Cho, Daniel L. Jenkin, and Simon L. Cornish. Feshbach resonances in ultracold ^{85}rb. *Phys. Rev. A*, 87:033611, Mar 2013.

[27] Andreas Neuzner, Matthias Körber, Stephan Dürr, Gerhard Rempe, and Stephan Ritter. Breakdown of atomic hyperfine coupling in a deep optical-dipole trap. *Phys. Rev. A*, 92:053842, Nov 2015.

[28] Daniel A. Steck. Rubidium 87 D line data. 2025. Revision 2.3.4, 8 August 2025.

[29] Y. A. Yang, Maya Miklos, Yee Ming Tso, Stella Kraus, Joonseok Hur, and Jun Ye. Clock precision beyond the standard quantum limit at 10^{-18} level. *Phys. Rev. Lett.*, 135:193202, Nov 2025.

[30] Sebastian Pucher, Sofus Laguna Kristensen, and Ronen M. Kroeze. ^{88} sr reference data, 2025.

[31] Martin M. Boyd. *High Precision Spectroscopy of Strontium in an Optical Lattice: Towards a New Standard for Frequency and Time*. PhD thesis, University of Colorado, Boulder, USA, 2007.

[32] Amani Kiruga, Charles Cheung, Dmytro Filin, Parinaz Barakhshan, Akshay Bhosale, Vipul Badhan, Bindiya Arora, Rudolf Eigenmann, and Marianna S. Safronova. Portal for high-precision atomic data and computation. *Computer Physics Communications*, 319:109951, 2026.

[33] Cheng Chin, Rudolf Grimm, Paul Julienne, and Eite Tiesinga. Feshbach resonances in ultracold gases. *Reviews of Modern Physics*, 82(2):1225–1286, April 2010.

[34] Jean Dalibard. Collisional dynamics of ultracold atomic gases. 2002.

[35] M. Egorov, B. Opanchuk, P. Drummond, B. V. Hall, P. Hannaford, and A. I. Sidorov. Measurement of s-wave scattering lengths in a two-component bose-einstein condensate. *Physical Review A*, 87(5), May 2013.

[36] Simon Sala and Alejandro Saenz. Theory of inelastic confinement-induced resonances due to the coupling of center-of-mass and relative motion. *Phys. Rev. A*, 94:022713, Aug 2016.

[37] J. P. D'Incao, Fatima Anis, and B. D. Esry. Ultracold three-body recombination in two dimensions. *Phys. Rev. A*, 91:062710, Jun 2015.

[38] Premjith Thekkeppatt. *A tale of two species: ultracold rubidium and strontium.* PhD thesis, Universiteit van Amsterdam, 2024.

[39] H. J. Metcalf and P. van der Straten. Laser cooling and trapping of atoms. *J. Opt. Soc. Am. B*, 20(5):887–908, May 2003.

[40] Rudolf Grimm, Matthias Weidemüller, and Yurii B. Ovchinnikov. Optical dipole traps for neutral atoms. *arXiv:physics/9902072*, 42:95–170, 1999.

[41] Markus Greiner. *Ultracold quantum gases in three-dimensional optical lattice potentials.* PhD thesis, Ludwig-Maximilians-Universität, München, 2003.

[42] R. Jáuregui, N. Poli, G. Roati, and G. Modugno. Anharmonic parametric excitation in optical lattices. *Physical Review A*, 64(3), August 2001.

[43] J Hecker Denschlag, J E Simsarian, H Häffner, C McKenzie, A Browaeys, D Cho, K Helmerson, S L Rolston, and W D Phillips. A bose-einstein condensate in an optical lattice. *Journal of Physics B: Atomic, Molecular and Optical Physics*, 35(14):3095–3110, July 2002.

[44] Kevin M. Jones, Eite Tiesinga, Paul D. Lett, and Paul S. Julienne. Ultracold photoassociation spectroscopy: Long-range molecules and atomic scattering. *Rev. Mod. Phys.*, 78:483–535, May 2006.

[45] Zhixin Liu and Radan Slavík. Optical injection locking: From principle to applications. *Journal of Lightwave Technology*, 38(1):43–59, 2020.

[46] T B Simpson, J M Liu, K F Huang, and K Tai. Nonlinear dynamics induced by external optical injection in semiconductor lasers. *Quantum and Semiclassical Optics: Journal of the European Optical Society Part B*, 9(5):765, oct 1997.

[47] Alessio Ciamei. *Taming ultracold RbSr and Sr2.* PhD thesis, Universiteit van Amsterdam, 2018.

[48] Daniel A. Steck. *Quantum and Atom Optics.* 2007. Revision 0.16.6, 17 October 2025.

[49] Nikolay V. Vitanov, Andon A. Rangelov, Bruce W. Shore, and Klaas Bergmann. Stimulated raman adiabatic passage in physics, chemistry, and beyond. *Rev. Mod. Phys.*, 89:015006, Mar 2017.

[50] Shinya Kato, Seiji Sugawa, Kosuke Shibata, Ryuta Yamamoto, and Yoshiro Takahashi. Control of resonant interaction between electronic ground and excited states. *Phys. Rev. Lett.*, 110:173201, Apr 2013.

Acknowledgments

Thank you Klaasjan for giving me the opportunity to join the "most fundamental experiment in the hallway" for my master's project. I had a great time and learned so many things. I really appreciated how honest, direct, and talkative you were, and thank you for your precise feedback.

Thank you, Florian, for letting me join your amazing group. I think it has been the best environment to develop my research skills. I am continually impressed by how much you know.

Digvijay, I can hardly imagine a better match. I always felt free to ask any question, and I really appreciated that you gave me real responsibilities on the experiment. I learned so much – you are an amazing supervisor. Beyond that, we shared so many highs and lows in the lab, and we became good friends! Thanks to Thom, Katy, and Roger for giving us the energy to work through the evenings ;).

Davide, thank you for the daily dose of southern European support, the technical advice, and the dinners. We became good friends, and knowing you were next door has always been a positive vibe.

Thanks to my neighbors Ivo, Yu Chih, and Alex for being so patient and kind in carefully answering all my questions. I really appreciate the time we spent together, inside and outside the lab. The same goes for Benedikt and Ananya, our neighbors on the other side of the corridor. Thanks, András, for the tips and tricks in and out of the lab, and thanks, Benoit, for letting me steal the spectrum analyzer even when you needed it. Thanks to the rest of the group for the support and kindness.

Elisa, you have been the AMEP person I've spent the most time with since the beginning. We shared a lot of struggle and fun, inside and outside of uni. We talked about everything – I admire (and fear!) the strength of your principles. I'm sorry I hyped you up so much about molecules; I hope you'll enjoy them :).

Luuk, you are so effective and passionate! I hope to learn something from you in the years to come.

Ale, Anezka, Chris, Hannah, Karel, Marte, and Tomas, you made these two years fly by. It has been great fun, and I feel so damn lucky.

Erik, you have been our cool Dutch daddy: you adopted us two years ago and you carefully carried us through to the end of these intense two years. I admire your strength and love humor.

A huge thank you goes to Cocky. The practical kindness, the simplicity, and the ease with which you accepted living with two Italians is still unbelievable to me. Thank you also for giving me the chance to live with Gabriele, even if just for a couple of months. G, you're one of the people I most enjoy spending time with.

Imagine moving to a new country without knowing anyone. You open the door of your new apartment and... you find your best friend. This is basically what happened with Jonas. I still cannot believe how lucky we have been.

Ellis, somehow you have been present in this experience from the very beginning. Thank you for your time and energy.

Thanks to my parents, you are the first spiritual and financial sponsors of this life-changing experience. Thank you Vale, you are always my fan number one.

Thanks, Nonna, again, for reminding everybody to feel blessed to be able to live the human experience.